Oxygen potential calculations for conventional and Cr-doped UO_2 fuels based on solid solution thermodynamics

Enzo Curti[a,] *, Dmitrii A. Kulik[a]

[a]Laboratory for Waste Management (LES), Nuclear Energy and Safety Division (NES),

Paul Scherrer Institut, CH-5232 Villigen PSI (Switzerland)

* Corresponding author. E-Mail address: enzo.curti@psi.ch

HIGHLIGHTS

- Solid solution thermodynamics was successfully applied to model chemical equilibrium in UO_2 fuels
- Cr-doping does not affect significantly the oxygen potential of UO_2 fuels
- Oxygen potentials are sensitive to thermodynamic properties of Mo in ε-particles
- Fuel-cladding interaction may affect oxygen potential
- Oxygen potentials increase with burnup and converge at $\geq$ 40 GWd/t_{iHM} to values 5-30 kJ/mol higher than the Mo/MoO_2 buffer

Keywords

Oxygen potential, solid solution, thermodynamics, doped fuel

Figures required in color:

Figs. 2, 3, 6, 7, 9

Abstract

The effect of Cr-doping on the oxygen potential of UO_2 fuels was studied through a comprehensive thermodynamic treatment, relying on the formulation of sublattice solid solutions for the uranium dioxide and for a five-component noble metal phase (Mo, Pd, Ru, Rh, Tc). The UO_2 phase includes dissolution of Pu, minor actinides (Am, Cm, Np), soluble fission products (La, Nd, Ce) and trivalent chromium. As far as possible, interaction parameters quantifying non-ideality were calibrated against published experimental data and models. In addition, a $(Sr,Ba)ZrO_3$ ideal solid solution and a number of stoichiometric solids were considered in the equilibrium calculations, as well as ideal gas. The GEM-Selektor code was used for the calculations, with the in-house Heracles database and applying the built-in Berman's formalism.

Ellingham diagrams were calculated for fuel inventories at burnups ranging from 1 to 60 GWd/t_{iHM}, over a temperature range (400 ^oC – 1400 ^oC) covering in-pile conditions in light water reactors. The results indicate that Cr-doping will not affect significantly the oxygen potential, except at very low burnup. The calculated oxygen potentials appear to be sensitive to molybdenum dilution in the noble metal phase, and to a minor extent to its non-ideality. On the contrary, the combined effect of Pu, minor actinides and lanthanides dissolution in UO_2 is small. From 20 GWd/t_{iHM} upwards, the calculated oxygen potentials enter the field of experimentally determined values. Above 40 GWd/t_{iHM}, they converge to limiting values about 5-30 kJ/mol higher than the oxygen potentials buffered by coexisting pure metallic Mo and pure MoO_2. Further calculations indicate that internal oxidation of the cladding (zirconium alloy) could considerably lower the oxygen potential.

1. Introduction

1.1 Background and objectives of this study

In recent years, the use of UO_2 fuels doped with small amounts of chromia has become customary in commercial Light Water Reactors (LWR). The dopant induces a coarsening of the UO_2 grain size up to about 60 μm and a higher densification during the fuel fabrication [1]. The larger grain size reduces Fission Gas Release (FGR), allowing reactors to be operated at higher power than with conventional UO_2 fuel and thus for a more efficient energy production. More importantly, the concentrations of volatile fission products in the fuel-sheath gap (such as iodine and cesium) and the yield strength of the fuel are reduced, minimizing the risk of cladding failures through stress corrosion cracking [2, 3].

A collaborative scientific project is currently ongoing in the framework of the Horizon 2020 EU program under the acronym *DisCo* (Modern spent fuel *Dis*solution and chemistry in failed *Co*ntainer conditions) mainly focusing on spent fuel degradation in a geological repository for radioactive waste [4]. The present contribution is embedded in *DisCo* ‘s modeling package. The major objective is to compare oxygen potentials of Cr-doped and non-doped UO_2 fuel during normal reactor operation in commercial LWRs, in order to predict possible consequences on spent fuel dissolution and on radionuclide release that may arise in a geological repository after containment failure. This objective is pursued by developing a comprehensive thermodynamic model for both types of fuels, capable of taking into account the effects of solid solution formation (in UO_2 and in minor phases) and of oxidation at the inner surface of zirconium alloy cladding, as functions of temperature and burnup. Because the focus of the study is on regular reactor operation, excluding the case of severe accidents, the temperature range of calculations was limited to 400-1400 ^{o}C. From the model, oxygen potentials vs. temperature plots (Ellingham diagrams) are calculated for both types of fuel.

The comparison of the predicted oxygen potentials will then allow assessing whether or not Cr-doped fuels would behave unfavorably under repository conditions.

1.2 The role of oxygen potential

For a system at chemical equilibrium, the partial molar Gibbs energy of oxygen, $\Delta\bar{G}_{O_2}$, is defined as the difference between the chemical potential of free molecular oxygen at a given total pressure *p* and absolute temperature *T*, and the same quantity at standard state (T^o=298.15 K, p^o= 1 bar) [5]. Hence, $\Delta\bar{G}_{O_2} \equiv \mu_{O_2} - \mu^o_{O_2} = RT\ln\left(f_{O_2}/p^o\right)$, where p^o is the standard state pressure (1 bar) and f_{O_2} is the oxygen fugacity. For the purpose of this application, the oxygen fugacity can be equated to the oxygen partial pressure, p_{O_2}, based on the approximation $f_{O_2} \cong p\ x_{O_2} \equiv p_{O_2}$, where p is the total pressure and $x_{O_2}$is the mole fraction of O_2 in the gas. This simplification is permissible since ideal gas at a low total pressure of 1 bar are assumed in this study. $\Delta\bar{G}_{O_2}$ is improperly termed "oxygen potential" in most of the literature, which generates confusion since this term actually defines μ_{O_2}. Because of the widespread use of this term for $\Delta\bar{G}_{O_2}$, however, it is maintained in this publication.

The oxygen potential primarily affects the O/M ratio (i.e. the hyper- or hypostoichiometry) of the uranium dioxide phase, which in turn is responsible for phenomena in the fuel that are highly relevant for reactor operation safety and radionuclide release in a geological repository [5, 6]. For instance, high oxygen potentials favor the oxidation of zirconium alloy at the internal cladding surface, thus increasing the risk of mechanical failures. Moreover, high oxygen potentials could lead to hyperstoichiometric O/M ratios in the UO_2 phase, reducing the thermal conductivity of the fuel and thus reactor performance. Hyperstoichiometry also increases the diffusivity of fission products, favoring high Fission Gas Release (FGR) and the segregation of volatile and water-soluble fission products such as Cs and I. These phenomena could lead to high Instant Release Fractions (IRF) after

containment failure and flooding with aqueous solution in a repository. Moreover, a faster UO_2 matrix dissolution rate is expected for hyperstoichiometric fuel [7, 8]. Finally, high oxygen potentials may also lead to the oxidation of multivalent radionuclides (e.g. ^{235}U, ^{239}Pu, ^{93}Mo, ^{126}Sn, ^{237}Np), making them more soluble in the aqueous environment of a geological repository. The latter aspects are the most relevant in the context of this contribution to the *DisCo* project, since they may affect the mobility of dose-relevant nuclides in a geological repository setup and ultimately increase the radiological doses calculated in safety assessments.

1.3 Previous work and model description

A few earlier studies have been carried out to model comprehensively LWR fuel behavior with the aim of determining oxygen potentials [9, 10]. In these studies, typical physical phenomena observed in LWR fuels (e.g., formation of fission gas bubbles, segregation of fission products) were modeled in combination with chemical reactions, predicting the formation of minor metallic and oxide phases. However, chemical reactions were modeled on the generalized assumption of simple ideal solid solution formation [10], which is hardly applicable to the UO_2 phase. Moreover, the origin of the underlying thermodynamic data was not documented sufficiently. Clearly, there is an urgent need to improve the chemical models in order to predict reliably oxygen potentials in UO_2 fuels.

In this study, the focus is on the accurate thermodynamic description of the fuel system. The effects of non-ideal mixing in UO_2 and noble metal solid solution (ε-particles) were considered accurately by calibrating interaction parameters against published experimental data or established mixing models (see Section 3). Segregation processes and transport phenomena were not treated explicitly, but they can to some extent be evaluated indirectly by carrying out calculations at different temperatures representative of the thermal gradient through LWR pellets.

The final model calculates complete thermodynamic equilibrium in a conventional or Cr-doped UO_2 fuel rod irradiated in a LWR, using detailed model inventories with a defined average burnup. It includes, besides stoichiometric solids, a complex UO_2 solution phase with U^{5+}, Cr^{3+}, Pu, minor actinides and lanthanides as minor solutes, a quinary (Mo, Pd, Rh, Ru, Tc) solid solution representing ε-particles, a binary $(Ba,Sr)ZrO_3$ phase representing a very simplified "grey phase" and an ideal gas phase. The calculations rely on sublattice solid solution models and the method of Gibbs energy minimization. They were carried out using the GEM-Selektor software [11, 12] with the in-house thermodynamic database HERACLES [13]. From the resulting equilibrium pO_2, oxygen potentials were derived as a function of temperature, allowing the construction of Ellingham diagrams. A detailed description of the thermodynamic model and HERACLES database, as well as a short review of alternative models/databases, is presented in Section 3.2 and Appendices A-D.

2. Crystal chemistry of UO_2 and Cr-defects formation

2.1 Sublattice structure of stoichiometric and hyperstoichiometric urania

Uranium (IV) oxide has a fluorite-type structure, which is characterized by three different crystallographic positions, generating three distinct sublattices: the anionic sublattice, the cationic sublattice and the interstitial sublattice [14]. In stoichiometric UO_2, the anionic and cationic sublattices are both fully occupied by oxygen anions (O^{2-}) and tetravalent uranium cations (U^{4+}), respectively. The interstitial sublattice (v_x) is defined by completely vacant U-equivalent positions. When UO_2 is subject to elevated pO_2 and foreign ions are incorporated, the occupancies of all three sublattices and the valence of uranium ions may change.

Specifically, diffusion of molecular oxygen through the interstitial sublattice leads to the formation of hyperstoichiometric urania [15]. This explains the strong dependence of UO_2 stoichiometry on oxygen partial pressure. As molecular oxygen diffuses into the UO_2 lattice,

it picks up electrons from U^{4+} and is converted to O^{2-}, thereby oxidizing U^{4+} to U^{5+}. Several experimental and simulation studies indicate that U^{4+} is oxidized to U^{5+}, not to U^{6+} [16, 17, 18].

At high degrees of hyperstoichiometry the so-called Willis defect complex forms, consisting of two interstitial oxygen ions occupying juxtaposed vacancies and two regular oxygen ions shifted along the (1 1 1) direction [5, 17, 19]. Apparently, the formation of Willis defects in UO_{2+y} starts at y > 0.01 [20] and should therefore not occur at the low degrees of hyperstoichiometry established in irradiated UO_2 fuel. Hypostoichiometry is more difficult to achieve in UO_2 and requires elevated temperatures in excess of 1300 ºC [5].

2.2 Cr defects formation in UO_2

Available X-ray absorption spectroscopy data indicate that the stable form of substituted chromium in UO_2 is Cr^{3+} [21, 22], i.e. the same oxidation state as for the Cr_2O_3 dopant used in the fabrication of Cr-doped fuel [1]. Atomistic studies [23, 24] indicate that the energetically most favored substitution mechanism of Cr^{3+} in stoichiometric UO_2 is incorporation into cation sites. Charge-compensation is achieved via formation of vacancies in the oxygen sublattice. For each pair of U^{4+} cations replaced by two Cr^{3+} cations, a single oxygen vacancy forms. The defect formation reaction, expressed in Kröger-Vink notation [25], is:

$$Cr_2O_3 + 2\,U_U^x + O_O^x \rightarrow 2\,UO_2 + 2\,Cr_U' + v_O^{\cdot\cdot} \qquad (1)$$

A similar substitution scheme was found to be the most favorable substitution mechanism in hyperstoichiometric urania (UO_{2+y}). However, a different charge-compensation mechanism is proposed, i.e. the annihilation of oxygen accommodated in the interstitial sublattice [23]:

$$Cr_2O_3 + 2\,U_U^x + O_i'' \rightarrow 2\,UO_2 + 2\,Cr_U' + v_i^x \qquad (2)$$

3. Thermodynamic modeling of conventional and Cr-doped UO_2 fuel

3.1 Selection of a solid solution model for the UO_2 phase

During irradiation, the UO_2 phase transforms to a multicomponent solid solution including Pu, minor actinides and lanthanides as solutes [26]. Some of these elements (U, Pu, Np) may occur in different oxidation states, adding further complexity. A central step for the thermodynamic description of the fuel system is thus the selection and implementation of an appropriate mixing model. Because the UO_2 structure consists of three distinct sites and mixing of species may occur both within and across the sites, an advanced sublattice model appears to be the most appropriate tool to treat solid solution formation in irradiated UO_2.

The GEM-Selektor code has built-in routines offering a large variety of options for the implementation of solid solution phases, ranging from simplest, one-site ideal solid solution models to advanced models for treating multisite multicomponent non-ideal solid solutions. For this study, the mixing model of Berman was selected [27, 28]. In a first step an UO_2 solid solution limited to the Cr-U-O compositional space was defined. Subsequently Pu, minor actinides and lanthanides were added as additional components. The reasons why this model was preferred to other well-established formalisms are discussed in Section 3.2.

3.2 Description and comparison of sublattice models

Sublattice models are compulsory whenever chemical species exchange in a solid at different crystallographic sites, as in the case of UO_2. It is therefore not surprising that they are widespread in thermodynamic descriptions of nuclear fuel. The theoretical foundations and formalism have been developed in all details by several authors, particularly for the special case of reciprocal solid solutions [29, 30, 31, 32, 33]. In a reciprocal solution a minimum of four species substitute independently on two distinct crystallographic sites. In such case, the compositional relations can be described by a square, the corners defining end-member compositions. Any given solution composition within the square can be quantified

alternatively by two mutually exclusive (i.e. reciprocal) end-member triangles, defined by the diagonals of the square. This property reduces the degrees of freedom of compositional and thermodynamic relations, which is known as "reciprocity relations" and leads to a well-defined simplified formalism in the thermodynamic description of such solid solutions.

A key result is that the activity coefficients of end-members in ideal reciprocal solutions may not be unity, in spite of the assumption of random mixing in the sublattices. For instance, given four species denoted as *Ta, Tb, Sa, Sb* that mix independently on sites I and II yielding a solid solution of the type $^{I}(Sa,Sb)_s\,^{II}(Ta,Tb)_t$ it can be demonstrated (see chapter 9.1.1 in [32]) that the chemical potential $\mu^{ss}_{Sa_sTa_t}$ of the end-member $^{I}(Sa)_s\,^{II}(Ta)_t$ in the solution is:

$$\mu^{ss}_{Sa_sTa_t} = \mu^{o}_{Sa_sTa_t} + RT\,ln[(y_{Sa})^s(y_{Ta})^t] + \Delta G^o_r[(1-y_{Sa})(1-y_{Ta})] + \Delta\bar{G}^{ex} \qquad (3)$$

where *s* and *t* are the stoichiometric coefficients ("site multiplicities"), y_{Sa} and y_{Ta} denote site fractions, $\mu^{o}_{Sa_sTa_t}$ is the standard chemical potential of pure $^{I}(Sa)_s\,^{II}(Ta)_t$, *R* is the gas constant and *T* absolute temperature. ΔG^o_r is the standard Gibbs energy of the reciprocal reaction and $\Delta\bar{G}^{ex}$ is the partial Gibbs excess energy, which quantifies non-ideality. Because the sum of the second and third terms in eq. 3 is not equal to the end-member mole fraction of $^{I}(Sa,Sb)_s\,^{II}(Ta,Tb)_t$, the reciprocal solid solution does not behave like an ideal solution with a single mixing site, although the enthalpic interactions among the substituting species sum up to zero (i.e. $\Delta\bar{G}^{ex} = 0$ in eq. 3).

Hillert [31, 34] systematically developed the formalism of sublattice reciprocal solutions, giving rise to the Compound Energy Formalism (CEF), which has been implemented in the well-known CALPHAD method [35]. In CEF, activity-composition relations are defined with respect to a reference Gibbs energy surface defined by the Gibbs energy of the pure end-

member compounds. The method is nowadays widely used in metallurgic and nuclear materials applications, including systems of direct interest for this study.

Guéneau et al. [36] developed a complete thermodynamic model of the U-Pu-O system assuming mixing in all three sublattices of the UO_2 fluorite structure, following pioneering work by Chevalier et al. [37]. A reciprocal solid solution was defined in which mixing of U^{3+}, U^{4+}, U^{6+}, Pu^{3+} and Pu^{4+} occurs in the cationic sublattice, while vacancies or interstitial oxygen were allowed to mix in the anionic and interstitial sublattices, respectively. The model was calibrated against a large number of compositional and oxygen potential data and allows calculating ternary phase diagrams over a large temperature range. The compositional range of this solid solution is however insufficient for the purpose of this study, which is to model the stable assemblage in irradiated LWR fuel rods as a function of temperature and burnup.

The thermodynamic treatment developed by Thompson et al. [38], also based on the CALPHAD method, is closer to the objectives of this study, as it aims at calculating the complete stable phase assemblage in UO_2 fuels. This model includes a complex UO_2 solid solution with 19 minor solutes (alkali, earth-alkali, lanthanides and tetravalent cations). Pu is apparently included only in the tetravalent form (a Pu_2O_3 end-member is missing) and hyperstoichiometry is modeled using the hexavalent uranium end-member (UO_3). The model also includes quinary noble metal solid solutions (in hcp and fcc modifications), U-noble metal compounds and various non-fluorite stoichiometric and binary oxides, some of which simulate perovskite-type oxides ("grey phase"). It was applied to calculate the phase assemblage of CANDU fuel with 175 GWd/t_{iHM} burnup, but no oxygen potential calculations were presented.

In the present study, the model of Berman [27, 28] is used, which is similar, though not identical, to the CEF. Berman's model is also a sublattice model that allows treating mixing of multiple species (including vacancies) on several sites; reciprocal terms can be used

optionally. Although less generalized and rigorous than CEF, it is more flexible since it allows defining end-members occupied by more than a single mixing species. For instance, it accepts the definition of an end-member with stoichiometry U_4O_9= $U^{4+}{}_2U^{5+}{}_2O_9$ in which the cationic sublattice is occupied by two different U species. This is not possible with the CEF method, which requires U_4O_9 to be described by two distinct "pure" end-members (e.g. UO_2 and $UO_{2.5}$).

In practice, the CEF is useful for systems with a limited number of components, for which a large set of experimental data allow simultaneous fitting of many required interaction parameters defining the $\Delta\bar{G}^{ex}$ term in eq.3. The system of interest here does not fulfill these requirements, since the number of required components is too large, and available experimental data are limited. Moreover, the need for atypical end-member forms with sites occupied by multiple species like U_4O_9 was dictated by the limited quality of data for pure U(V) compounds, see Section 3.3. Thompson et al. [38] used the hexavalent uranium compound $U^{VI}O_3$ to model hyperstoichiometry in the urania solid solution. However, since recent spectroscopic studies have made clear that U^{4+} oxidizes to U^{5+} (not to U^{6+}) [16, 17, 18] in UO_{2+x}, selecting an U(V) end-member appears to be more appropriate.

Therefore, Berman's model, the formal treatment of which is presented in Appendix D, is used in this study. The following Sections describe the implementation of the model with increasing degrees of complexity, starting from the ternary system Cr-U-O, then adding other fission products and actinides as solutes of the uranium dioxide phase. Finally, a quinary noble metal solid solution (system Mo-Pd-Rh-Ru-Tc) and the binary $(Sr,Ba)ZrO_3$ are defined.

As anticipated in Section 1.3, the calculations were performed using the GEM-Selektor code (v. 3.4.2) implemented with the in-house HERACLES database and selected Cr-data (Appendix B). Alternative databases exist, but either they are not freely available (e.g. the full TAF-ID database is available only to project signatories [39]), or they are incomplete (e.g. MEPHISTA-15 [40] does not include elements of interest such as Tc, Se, I, Nd, Am, Cm, Np,

Pd, Rb, Rh, Cr) or they are provided in a format that cannot be implemented in GEM-Selektor without a major effort beyond the scope of this study (RMC Fuel Thermodynamic Treatment [41]). A survey of the data sources listed in Reference [41] indicates that many of them are the same as those used to compile the HERACLES database, thus one expects calculations with either database to yield equivalent results.

3.3 Solid solution definition and calibration for urania: Cr-U-O system

Fig. 1 shows the compositional space of the ternary Cr^{III}-U^{IV}-U^{V}-O system. Each corner marked with a dot symbol defines a potential end-member stoichiometry, expressed both as bulk stoichiometry and site formula. The highlighted triangle defines the selected end-member stoichiometries, chosen based on the criteria outlined below.

The selection of an end-member including pentavalent uranium was limited by the availability and quality of thermodynamic data. $U^{V}O_{2.5}$, was discarded since the data are unreliable and even the structure of this compound is uncertain [42]. $U^{V}Cr^{III}O_4$ had also to be excluded because, although an orthorhombic compound with this stoichiometry is known [43], its thermodynamic properties are not sufficiently assessed.

Therefore, a mixed U^{IV}/U^{V} stoichiometry corresponding to U_4O_9 was selected as end-member due to the availability of well-assessed thermodynamic data for compounds with this stoichiometry over the whole temperature range of interest [44, 45]. Moreover, the structures of all three known polymorphs (α, β, γ-U_4O_9) are closely related to the fluorite-type UO_2 lattice [46, 47], which is not the case of $U^{V}Cr^{III}O_4$.

In Fig. 1, square brackets indicate site stoichiometries showing the occupancies of all moieties considered (i.e. Cr^{3+}, U^{4+}, U^{5+} and vacancies ‘v’) in all three sublattices (cationic, anionic, interstitial). Each sublattice is comprised between two vertical bars. For instance, the site formula of the end-member with bulk stoichiometry ½(U_4O_9) shows that the cationic

sublattice is half occupied by U^{4+} and half by U^{5+} cations, the anionic sublattice is fully filled with O^{2-} ions and the interstitial sublattice is half-filled with O^{2-} ions and half vacant.

The Berman-type Cr^{III}-U^{IV}-$U^{V}O_{2+y}$ solid solution delimited by the highlighted triangle in Fig. 1 was formulated in GEM-Selektor by defining 11 pseudo-ternary interaction parameters, each allowing for the definition of three coefficients describing temperature dependence. As shown later, three non-zero, temperature independent parameters proved to be sufficient to fit all experimental data used to calibrate the model (Table 1).

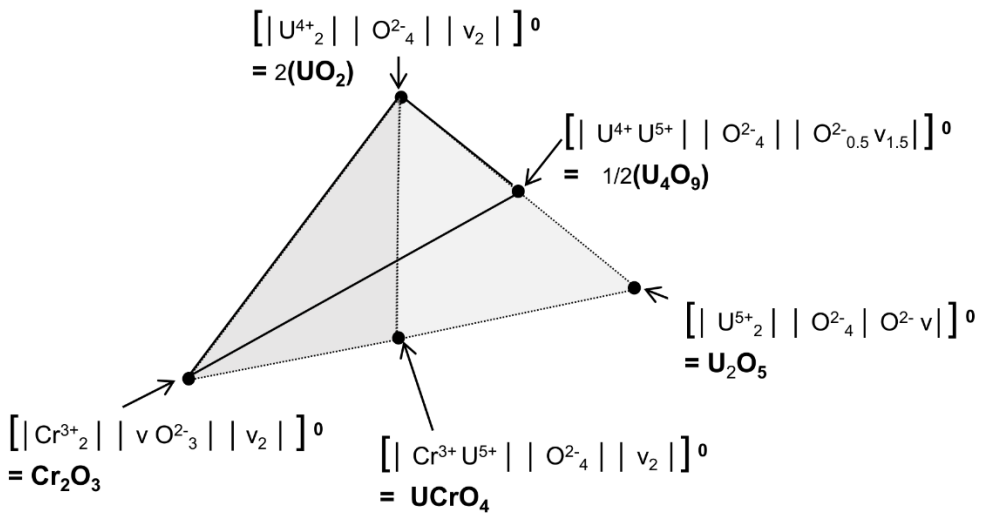

Fig. 1. Compositional diagram of the U-Cr-O system showing the three selected end-member stoichiometries (triangle highlighted with thick lines) describing Cr-doped UO_2 as ternary solid solution with three sublattices. Dotted triangles indicate discarded end-member combinations.

The non-ideality parameter describing interaction of Cr^{3+} with U^{4+} in the cation sublattice ($W_{Cr\_U4\_U4}$) was obtained by fitting experimental data on Cr-solubility in UO_2 reported by Riglet-Martial et al. [21]. The fitting procedure is shown in Fig. 2, where the Cr-solubility data are plotted as mole fractions of Cr in UO_2 as a function of the measured equilibrium pO_2.

The corresponding best-fit lines were generated by manual adjustment of the $W_{Cr\_U4\_U4}$ parameter value at the specified temperature. Each fit was obtained by carrying out a sequence of GEM-Selektor calculations (typically 50) in which the amount of O_2 in a closed system containing 1 mole of UO_2 and a small excess of metallic Cr is progressively increased. Each color-coded fit line defines, for a specific temperature, the log pO_2–Cr mole fraction values at which the Cr-UO_{2+y} solid solution is in equilibrium either with metallic Cr (steep segments to the left of the discontinuity) or with pure Cr_2O_3 (quasi-horizontal segments to the right).

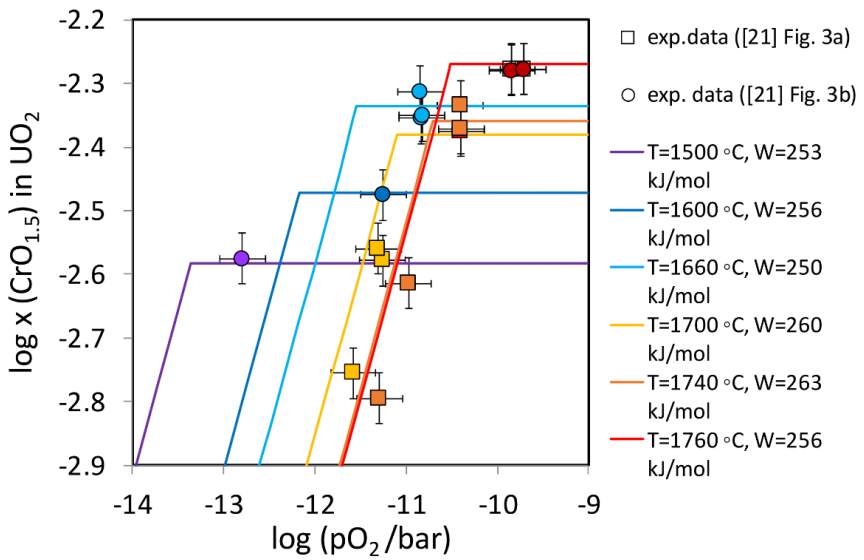

Fig. 2. Determination of $W_{Cr\_U4\_U4}$ parameter through fitting of Cr-solubility data from Riglet-Martial et al. [21].

The fitted values of $W_{Cr\_U4\_U4}$ in kJ/mol are indicated in the legend of Fig. 2. It is evident that high positive parameters are required to fit the small solubilities of Cr in stoichiometric UO_2, ranging between 0.1 and 1 mol %. The ideal solid solution model would predict equilibrium mole fractions of Cr in UO_2 that are greatly in excess of these experimental data and is therefore clearly inadequate. The fitted $W_{Cr\_U4\_U4}$ -values are remarkably independent of temperature, as indicated by the low standard deviation of the calculated average (261.8 ±

6.6 kJ/mol) and close to the energy of dissolution of Cr(III) in UO_2 (ΔH_r = 294.3 kJ/mol) inferred via atomistic simulations by Middleburgh et al. [23]. For the fuel calculations presented in Section 4, the value of 255 kJ/mol obtained at 1500 ºC, the temperature closest to fuel conditions in LWRs during neutron irradiation, was adopted.

Two other interaction parameters referring to the U-Cr-O subsystem are reported in Table 1, describing the interactions between U^{4+} and U^{5+} upon mixing in the cation sublattice of hyperstoichiometric urania (denoted $W_{U4\_U5\_U5}$ and $W_{U4\_U4\_U5}$). These parameters were derived by fitting the experimental data by Nakamura and Fujino [48], who measured pO_2 as a function of hyperstoichiometry over a wide temperature range (500 ºC – 1400 ºC). Using the GEMSFIT package [49], a simple combination of interaction parameters was found ($W_{U4\_U5\_U5}$ = $W_{U4\_U5\_U5}$ = 100 kJ/mol) that reproduces reasonably Nakamura and Fujino's data at low hyperstoichiometry (y < 0.02) between 500ºC and 1400 ºC (Fig. 3). This fulfills the requirements for the purpose of this study, since off-stoichiometry in irradiated UO_2 fuels never exceeds a few permils [50].

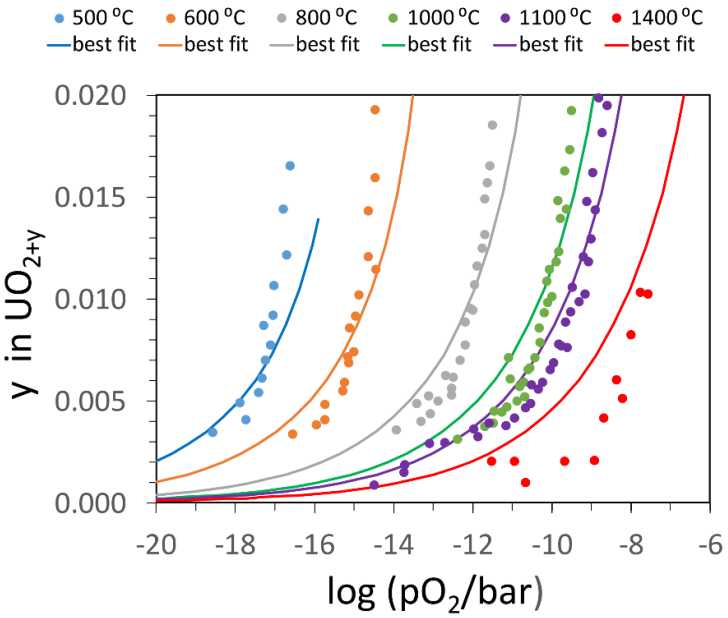

Fig. 3. Fits of data by Nakamura and Fujino [48] to determine interaction parameters for the $(UO_2)_2$-$(UO_{2.25})_2$ binary solid solution.

3.4 Solid solution definition and calibration for urania: extension to the Cr-U-O-Pu-Np-Am-Cm-Nd-Ce-La system

A further necessary step for defining a realistic uranium dioxide solid solution in irradiated LWR fuel is its extension to include fission products and actinides that dissolve significantly in the UO_2 lattice. In contrast to chromium, lanthanides and transuranics substitute easily in the cation sublattice of UO_2 due to similar ionic radii and their chemical affinity to U^{4+}. The formulation of a realistic solid solution for UO_{2+y} should therefore also include mixing with species such as Am^{3+}, $Ce^{3+/4+}$, Cm^{3+}, La^{3+}, Nd^{3+}, $Np^{4+/5+}$, $Pu^{3+/4+}$. To this aim the urania solid solution was extended to include the following 17 end-members: Am_2O_3, Ce_2O_3, $(CeO_2)_2$, Cm_2O_3, Cr_2O_3, La_2O_3, Nd_2O_3, $(NpO_2)_2$, $(NpO_{2.5})_2$, Pu_2O_3, $(PuO_2)_2$, $(UO_2)_2$ and $(UO_{2.25})_2$.

The complete application of CEF or Berman's model would require for such a system a prohibitive number of interaction parameters. Even with binary indexation and mixing on a single site, as much as 78 interaction coefficients would be needed. Clearly, such an implementation is not practicable for a multi-element system like irradiated nuclear fuel. Thus, simplifications and approximations were introduced in order to reduce the number of parameters. Specifically, because all aforementioned end-members, except $(UO_2)_2$, are minor and all cations mix in the same sublattice, a single binary coefficient, describing the interaction each dissolved cationic species with the predominant U^{4+} cation, was considered to be sufficient. This reduces the total number of interaction parameters to 18.

In a first step, attempts were made to determine the interaction parameter describing the interaction of Nd^{3+} with U^{4+} by fitting the oxygen potential data of Une and Oguma [51] for $Nd_xU_{1-x}O_{2\pm y}$ (x=0.14), using a ternary solid solution phase including Nd_2O_3, $(UO_2)_2$, $(UO_{2.25})_2$ as end-members. However, it was not possible to reproduce the typical sigmoidal shape (centred on O/M=2.00) of the experimental oxygen potential curves. The "best fit", obtained by setting $W_{Nd\_U4\_U4}$ = +20 kJ/mol, is shown as dashed line in Fig. 4 for the data at 1500 ^{o}C.

This ternary solid solution only reproduces the hyperstoichiometric part of the data but fails in the hypostoichiometric section, where far too low O/M ratios are predicted. The oxygen potentials decrease slowly from O/M=2.0 to 1.95 and then rapidly fall to a limiting O/M of 1.93 related to the stoichiometric coefficient (x=0.14) of the $Nd_xU_{1-x}O_{2\pm y}$ compound used for the measurements. It arises from choosing Nd_2O_3 as end-member, which implies a substitution mechanism through which a single oxygen vacancy is created for each pair of Nd^{3+} added, yielding y = (1-0.14)/2 =0.93. This result is a clear indication that the selection of the three aforementioned components is not sufficient to describe thermodynamically the $Nd_xU_{1-x}O_{2\pm y}$ solid solution.

In order to shift the dashed curve in Fig. 4 to the right, so that O/M ratios only barely below 2.00 are obtained, one needs to assume a substitution mechanism that keeps more oxygen in the lattice, e.g. the coupled substitution of one Nd^{3+} and one U^{5+} for two U^{4+} ions. This mechanism does not require formation of oxygen vacancies and thus it does not reduce the O/M ratio. Thermodynamically, this substitution can be rationalized as a new end-member with stoichiometry $Nd^{III}U^{V}O_4$, which was added to the aforementioned three, eventually yielding a quaternary solid solution for $Nd_xU_{1-x}O_{2\pm y}$.

Although no thermodynamic data are available for this end-member (since there is no known phase with this composition), it was possible to obtain values for the standard-state Gibbs energy of formation and interaction parameters that fit satisfactorily the curve of Une and Uguma [51] at 1500 ºC (continuous line in Fig. 4). This was achieved by first determining standard-state formation properties from pure oxide reactions, then adjusting by trial and error the derived Gibbs energy of formation until a satisfactory fit of the oxygen potential data was achieved. Similar successful fits (not shown) were obtained for analogous data at 1300 ºC and 1000 ºC. The same strategy (i.e. formulation of a $La^{III}U^{V}O_4$ end-member) was followed to reproduce successfully oxygen potential data for $La_xU_{1-x}O_{2\pm y}$ (x=0.05) between 900 ºC and 1100 ºC (Fig. 5).

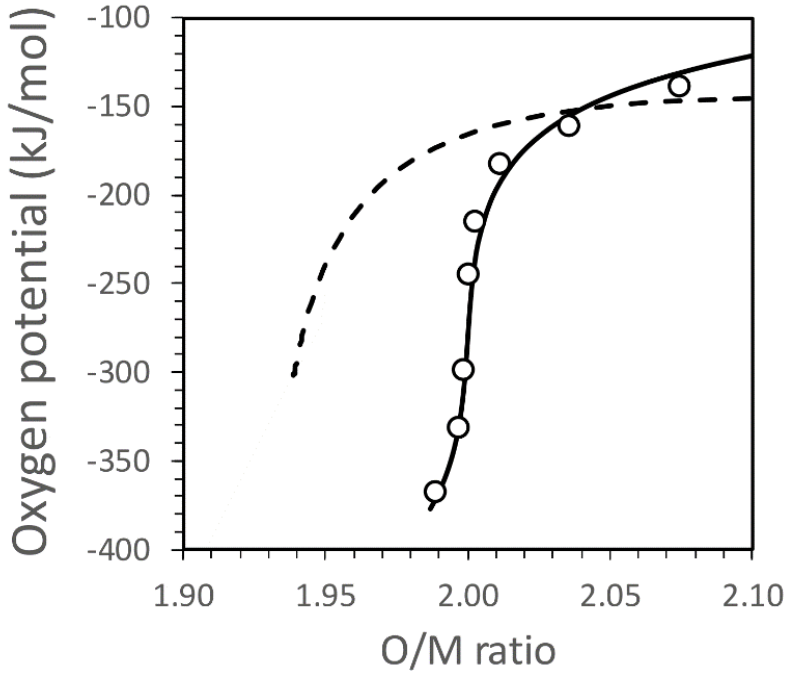

Fig. 4. Best fits of oxygen potential data from Une and Uguma [51] for $Nd_xU_{1-x}O_{2\pm y}$ (x=0.14) measured at 1500 ºC, using a ternary (dashed line) and a quaternary solid solution (continuous line).

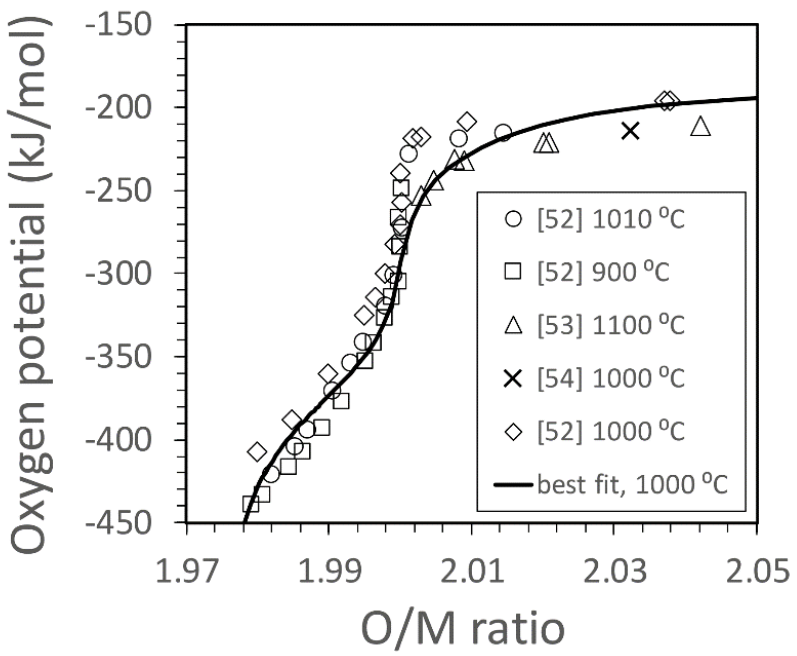

Fig. 5. Fit of oxygen potential data [52, 53, 54] for $La_xU_{1-x}O_{2\pm y}$ (x=0.05) measured between 900 ºC and 1100 ºC. The fit was calculated for T=1000 ºC.

After calibration of the $Nd^{III}U^{V}O_4$ and $La^{III}U^{V}O_4$ end-members, additional analogous components were defined for Am^{3+}, Cm^{3+}, Ce^{3+} and Pu^{3+}. In the absence of experimental data, the thermodynamic properties of these components were defined assuming that oxygen potential curves for the corresponding $Me_xU_{1-x}O_{2\pm y}$ are similar to those determined for $Nd_xU_{1-x}O_{2\pm y}$ (x=0.14), i.e. the Nd data of Fig. 4 were used for determining the Gibbs energies of $Am^{III}U^{V}O_4$, $Cm^{III}U^{V}O_4$, $Ce^{III}U^{V}O_4$ and $Pu^{III}U^{V}O_4$. This is obviously an approximation relying on the well-known chemical analogy between trivalent actinides and trivalent lanthanides [55, 56], frequently used to extrapolate unknown elemental properties within this series.

This calibration and simplification procedure eventually allowed us to define a 19 end-members urania solid solution comprising 17 distinct species mixing over three sublattices and only 24 non-zero interaction parameters to describe non-ideality (Table 1).

It must be realized that, unlike well-assessed subsystems such as U-Pu-O which reproduce experimental data over large compositional and temperature ranges with great fidelity [36], the model developed here represents a provisional compromise in the expectation of a more precise thermodynamic treatment for the compositionally much more complex spent fuel system. This goal will be achievable only when a large set of data relating realistic UO_2 fuel compositions to oxygen potentials will become available. In this sense, the present treatment bears resemblances to that of Thompson et al. [38].

3.5 Solid solution definition of noble metal inclusions

Known minor phases formed in LWR fuels by fission products incompatible with the UO_2 structure are micro-phases called ε-particles (or “white inclusions”) [57]. These are metallic alloys mainly consisting of the five metals Mo, Ru, Tc, Rh and Pd, with Mo and Ru as dominating constituents. Kaye [58, 59] studied the thermodynamic properties of these phases in detail, ending up in a quantitative assessment of the five-component liquid phase

and three solid structural modifications (fcc, bcc and hcp). Temperature-dependent functions of the excess Gibbs energy derived from these studies are reported in the RMC database [41]. Inspection of the equations showed however that the form of these functions is not amenable to any of the solid solution models currently implemented in GEM-Selektor.

It is nonetheless possible to "transfer" the RMC model for ε-particles to the Berman formalism implemented in GEM-Selektor. To this aim, the partial derivatives of the excess Gibbs energy expressions reported by Thompson et al. [41] were first calculated to derive activity functions for each end-members of the quinary ε-phase solid solution. The so-calculated activities were then fitted manually by varying the Berman interaction parameters. This time-consuming procedure (described in Appendix E) was applied to evaluate the effect of non-ideality on the oxygen potential for selected calculations (see Section 4.1 and Fig. 7). Furthermore, only the hexagonal (hcp) phase was considered, since this is the only modification formed under normal operating conditions in nuclear reactors operated with UO_2 fuels [59, 60]. All other calculations involving ε-phase solid solutions were carried out using the ideal mixing model.

3.6 Minor oxides

According to Kleykamp [57], the "grey phase" is a generic term for different types of ill-defined minor oxide precipitates. They can be best explained as a multi-component, perovskite-structure phase with complete miscibility in the pseudo-binary system $(Ba,Sr)(Zr,U,Pu)O_3$ [61]. Because the chemical characterization and thermodynamic properties of minor oxides in UO_2 fuels are still insufficiently known, it is customary to treat these phases as an assemblage of stoichiometric oxide phases [38]. Here the same approach is followed, except for $BaZrO_3$ and $SrZrO_3$, which are treated as ideal solid solution phase with stoichiometry $(Ba,Sr)ZrO_3$.

“Grey phases” are usually detected only in spent fuel from high-breeder reactors, so that even their occurrence in LWR fuels has been questioned [62]. This implies that only tiny amounts (if any) are formed in LWR reactors. The calculations discussed in Section 4 indicate that the maximum amounts expected to form are indeed only 1-2 mol %, which is about 2-3 times less than the predicted amount of ε-particles. The molar amounts of Pu and U that could be bound to “grey phases” would be even smaller because these elements share the same site with Zr. Therefore, it can be anticipated that the impact of perovskite-type oxides on the oxygen potential should be negligible.

Table 1. Description of the 19 end-members UO_2 solid solution according to Berman's sublattice model.

End members (components)
(a) bulk stoichiometries: Am_2O_3, $AmUO_4$, Ce_2O_3, $CeUO_4$, $(CeO_2)_2$, Cm_2O_3, $CmUO_4$, Cr_2O_3, La_2O_3, $LaUO_4$, Nd_2O_3, $NdUO_4$, $(NpO_2)_2$, $(NpO_{2.5})_2$, Pu_2O_3, $PuUO_4$, $(PuO_2)_2$, $(UO_2)_2$, $(UO_{2.25})_2$
(b) sublattice formulae: $\{\lvert Am^{3+}{}_2\rvert\lvert v\ O^{2-}{}_3\rvert\lvert v_2\rvert\}$, $\{\lvert Am^{3+}U^{5+}\rvert\lvert O^{2-}{}_4\rvert\lvert v_2\rvert\}$, $\{\lvert Ce^{3+}{}_2\rvert\lvert v\ O^{2-}{}_3\rvert\lvert v_2\rvert\}$, $\{\lvert Ce^{3+}U^{5+}\rvert\lvert O^{2-}{}_4\rvert\lvert v_2\rvert\}$, $\{\lvert Ce^{4+}\rvert\lvert O^{2-}{}_2\rvert\lvert v\rvert\}_2$, $\{\lvert Cm^{3+}{}_2\rvert\lvert v\ O^{2-}{}_3\rvert\lvert v_2\rvert\}$, $\lvert Cm^{3+}U^{5+}\rvert\lvert O^{2-}{}_4\rvert\lvert v_2\rvert\}$, $\{\lvert Cr^{3+}{}_2\rvert\lvert v\ O^{2-}{}_3\rvert\lvert v_2\rvert\}$, $\{\lvert La^{3+}{}_2\rvert\lvert v\ O^{2-}{}_3\rvert\lvert v_2\rvert\}$, $\lvert La^{3+}U^{5+}\rvert\lvert O^{2-}{}_4\rvert\lvert v_2\rvert\}$, $\{\lvert Nd^{3+}{}_2\rvert\lvert v\ O^{2-}{}_3\rvert\lvert v_2\rvert\}$, $\lvert Nd^{3+}U^{5+}\rvert\lvert O^{2-}{}_4\rvert\lvert v_2\rvert\}$, $\{\lvert Np^{4+}\rvert\lvert O^{2-}{}_2\rvert\lvert v\rvert\}_2$, $\{\lvert Np^{5+}\rvert\lvert O^{2-}{}_2\rvert\lvert v_{1.5}\ O_{0.5}\rvert\}_2$, $\{\lvert Pu^{3+}{}_2\rvert\lvert v\ O^{2-}{}_3\rvert\lvert v_2\rvert\}$, $\{\lvert Pu^{3+}U^{5+}\rvert\lvert O^{2-}{}_4\rvert\}$, $\{\lvert Pu^{4+}\rvert\lvert O^{2-}{}_2\rvert\lvert v\rvert\}_2$, $\{\lvert U^{4+}\rvert\lvert O^{2-}{}_2\rvert\lvert v\rvert\}_2$, $\{\lvert U^{4+}{}_{0.5}\ U^{5+}{}_{0.5}\rvert\lvert O^{2-}{}_2\rvert\lvert v_{0.75}\ O^{2-}{}_{0.25}\rvert\}_2$

Mixing species
cationic sublattice: Am^{3+}, Ce^{3+}, Ce^{4+}, Cm^{3+}, Cr^{3+}, La^{3+}, Nd^{3+}, Np^{4+}, Np^{5+}, Pu^{3+} , Pu^{4+}, U^{4+}, U^{5+} anionic sublattice: O^{2-}, v interstitial sublattice: O^{2-}, v

Interaction parameter	Value [kJ/mol]	Sublattice	Minor moiety	Major moiety
$W_{Cr\_U4\_U4}$	255	cationic	Cr^{3+}	U^{4+}
$W_{U4\_U5\_U5}$	100	cationic	U^{4+}	U^{5+}
$W_{U4\_U4\_U5}$	100	cationic	U^{5+}	U^{4+}
$W_{Ce4\_U4\_U4}$	0	cationic	Ce^{4+}	U^{4+}
$W_{Pu4\_U4\_U4}$	0	cationic	Pu^{4+}	U^{4+}
$W_{Ce3\_U4\_U4}$	0	cationic	Ce^{3+}	U^{4+}
$W_{La\_U4\_U4}$	0	cationic	La^{3+}	U^{4+}
$W_{Nd\_U4\_U4}$	0	cationic	Nd^{3+}	U^{4+}
$W_{Pu3\_U4\_U4}$	0	cationic	Pu^{3+}	U^{4+}
$W_{Pu4\_U4\_U4}$	0	cationic	Pu^{4+}	U^{4+}
$W_{Np4\_U4\_U4}$	0	cationic	Np^{4+}	U^{4+}
$^*W_{Np5\_U4\_U4}$	100	cationic	Np^{5+}	U^{4+}
$W_{Cm\_U4\_U4}$	0	cationic	Cm^{3+}	U^{4+}
$W_{Am\_U4\_U4}$	0	cationic	Am^{3+}	U^{4+}
$W_{Am\_U5\_U5}$	450	cationic	Am^{3+}	U^{5+}
$W_{Ce3\_U5\_U5}$	350	cationic	Ce^{3+}	U^{5+}
$W_{Cm\_U5\_U5}$	450	cationic	Cm^{3+}	U^{5+}
$W_{Pu3\_U5\_U5}$	350	cationic	Pu^{3+}	U^{5+}
$W_{Nd\_U5\_U5}$	350	cationic	Nd^{3+}	U^{5+}

Table 1 - continued

$W_{La\_U5\_U5}$	350	cationic	La^{3+}	U^{5+}
$W_{O1\_O1\_Va1}$	0	anionic	vacancy	O^{2-}
$W_{O1\_Va1\_Va1}$	0	anionic	vacancy	vacancy
$W_{Va2\_Va2\_O2}$	0	interstitial	O^{2-}	vacancy
$W_{Va2\_O2\_O2}$	0	interstitial	vacancy	O^{2-}

*This parameter was set +100 kJ/mol as for the previously calibrated U^{V}-U^{IV} parameter.

3.7 Model inventories

Table 2 shows the four elemental fuel compositions considered for the thermodynamic calculations. Two sets of fuel inventories for Pressurized Water Reactors (PWR) are given in two variants, one for non-doped UO_2 fuel, the other for fuel doped with 1 mol % Cr (added as Cr_2O_3). Compositions A and C were derived from the inventory given in Table XV of Ferry et al. [63]. They refer to PWR fuel with a burnup of 60 GWd/t_{iHM}, 2 years after download. Compositions B and D represent instead 60 GWd/t_{iHM} PWR fuel inventories at download time and were obtained from the webKORIGEN++ code, available at the Nucleonica web site [64]. Minor Rare Earth Elements (REE) in the inventories that are not included in the HERACLES database were distributed in equal proportions between Nd and La. The differences between the two inventory sets are minor, indicating that compositional changes due to decay during the very first years after download are small.

Table 2. Model inventories used in thermodynamic calculations for conventional and Cr-doped UO_2 fuels with average burnup of 60 GWd/$_{iHM}$, given in mol % with respect to initial U*. The rightmost column indicates in which of the phases included in our model a given element may partition.

	non-doped		**Cr-doped**		**Phases****
	A	**B**	**C**	**D**	
Cr	0.00	0.00	1.00	1.00	*UO_2*/ Cr / Cr_2O_3 / $CeCrO_3$
U	92.32	92.61	91.40	91.68	*UO_2*
Am	0.05	0.04	0.05	0.04	*UO_2*
Ba	0.25	0.24	0.25	0.23	*(Ba,Sr)ZrO_3* / $BaMoO_4$
Ce	0.36	0.39	0.36	0.39	*UO_2* /$CeCrO_3$
Cm	0.02	0.02	0.02	0.02	*UO_2*
Cs	0.42	0.43	0.42	0.42	Cs_2MoO_4
I	0.04	0.04	0.04	0.04	RbI / *gas*
Kr	0.09	0.09	0.09	0.09	*gas*
La	0.40	0.39	0.40	0.39	*UO_2*
Mo	0.75	0.70	0.75	0.69	*ε-phase* / MoO_2/ $BaMoO_4$ / Cs_2MoO_4
Nd	0.81	0.73	0.80	0.73	*UO_2*
Np	0.09	0.10	0.09	0.09	*UO_2*
Pd	0.36	0.32	0.35	0.31	*ε-phase*
Pu	1.26	1.20	1.24	1.19	*UO_2*
Rb	0.08	0.08	0.08	0.08	*ε-phase* /RbI / Rb_2O / *gas*
Rh	0.08	0.07	0.08	0.07	*ε-phase*
Ru	0.50	0.52	0.50	0.52	*ε-phase* / $RuSe_2$ / $RuTe_2$
Se	0.01	0.01	0.01	0.01	$RuSe_2$ / *gas*
Sr	0.19	0.20	0.19	0.20	*(Ba,Sr)ZrO_3*
Tc	0.16	0.16	0.16	0.16	*ε-phase*
Te	0.09	0.05	0.09	0.05	$RuTe_2$ / *gas*
Xe	0.85	0.83	0.84	0.82	*gas*
Zr	0.80	0.78	0.79	0.78	ZrO_2 / *(Ba,Sr)ZrO_3*

* This implies that total O in the system is exactly 200 mol % using this scale.
** Multicomponent phases (solid solutions and gas) are typed in italics.

4. Results and discussion of thermodynamic calculations

4.1 Main results and interpretation for 60 GWd/t_{iHM} fuel

The main results of the thermodynamic equilibrium calculations for PWR Cr-doped UO_2 fuel with 60 GWd/t_{iHM} burnup (Composition C, Table 2) are shown in Fig. 6 and Fig. 7. The former illustrates the equilibrium amounts of pure solids, solid solution end-members and gaseous Te as a function of temperature for the fully optimized model (i.e. including the three solid solutions defined in the preceding section). The corresponding oxygen potentials are shown in the Ellingham diagram of Fig. 7 as curve labeled '3 ss' along with two other calculations discussed later, and with the oxygen potential lines constrained by the pure Mo metal - pure MoO_2 and pure Cr metal - pure Cr_2O_3 equilibria.

When Fig. 6 is analysed from one side to the other of the T-axis, reactions that may occur during reactor irradiation with increasing temperature (i.e. from the pellet rim to the pellet centre) can be identified. The onset of such reactions is typically marked by sharp, correlated discontinuities in the amounts of specific phases or solid solution components (vertical dotted lines in Fig. 6) and can be recognized by the mirror-symmetrical evolution of reactants and products curves. The analysis of this plot led us to identify a sequence of reactions with increasing temperature, listed in Table 3. All reactions (with the exception of disproportionation reaction 6) produce or consume O_2(g) and may therefore affect the oxygen potential of the fuel.

Up to 660 ^{o}C, the oxygen partial pressure is controlled by the Mo(ss)/MoO_2(cr) system (reaction 1). Between 660 ^{o}C and 780 ^{o}C a more complex equilibrium, involving formation Ba molybdate, metallic Mo and zirconia at the expense of Mo^{IV} oxide and Ba zirconate, takes this role (reaction 2). From about 800 ^{o}C onward, the oxygen partial pressure is controlled by the interplay of reactions 3, 4, 5 and 7, which all involve equilibria among the three solid solutions defined in the thermodynamic model.

Equilibria 1, 2 and 3 illustrate the importance of molybdenum in controlling pO_2. These reactions control the oxygen potential up to about 1000 ºC, and it is only at higher temperatures that the reactions taking place in the UO_2 solid solution phase (reactions 4, 5 and 7) start to play a major role, together with equilibrium 3. Note that the interplay of these equilibria is complex and leads repeatedly to a change in the direction of reaction 3 (therefore a double arrow is used for this reaction in Table 3). These reversals cause changes from positive to negative slopes of the reactants ZrO_2(cr) and $BaMoO_4$(cr) curves in Fig. 6, e.g. between 1000 ºC and 1280 ºC, implying that these compounds are no longer products but reactants in reaction 3.

Fig. 6 also reveals that $Ce^{III}U^{V}O_4$ is the predominant cerium end-member in UO_2 up to 1300 ºC. Only at higher temperatures the $Ce^{III}{}_2O_3$ and $Ce^{IV}O_2$ end-members become majoritarian. The sharp decrease of the $Ce^{III}U^{V}O_4$ fraction in the UO_2 phase correlates with the steep increase of $Ce^{III}{}_2O_3$ and $U^{IV}U^{V}O_{4.5}$, according to the pO_2-dependent reaction 7. This transition occurs within a small temperature interval (1270 ºC - 1300 ºC) and corresponds to the change in the Nd substitution mechanism discussed in Section 3.4 for $Nd^{III}{}_xU_{1-x}O_{4\pm y}$ compounds. Analogous transitions reactions take place at similar temperatures for the other trivalent species considered.

Table 3. Main reactions predicted across the temperature range 400 ºC -1400 ºC for the optimized calculation ('3 ss') discussed in the text and illustrated in Fig. 6. Reaction arrows point in the direction of increasing temperature.

Reaction	**#**	**T /ºC**
$Mo^0(ss) + O_2(g) \rightarrow Mo^{IV}O_2(cr)$	1	400- 660
$2\ Mo^{IV}O_2(cr) + BaZrO_3(ss) \rightarrow 1/2\ O_2(g) + BaMo^{VI}O_4(cr) + Mo^0(ss) + ZrO_2(cr)$	2	660- 780
$BaZrO_3(ss) + Mo^0(ss) + 3/2\ O_2(g) \leftrightarrow ZrO_2\ (cr) + BaMo^{VI}O_4(cr)$	3	780-1400
$2\ Ce^{III}U^{V}O_4(ss) + 1/4\ O_2(g) \rightarrow 2\ Ce^{IV}O_2(ss) + U^{IV}U^{V}O_{4.5}(ss)$	4	800-1250
$2\ U^{IV}O_2(ss) + 1/4\ O_2(g) \rightarrow U^{IV}U^{V}O_{4.5}(ss)$	5	1250-1400
$Ru^{IV}Te^{-II}2(cr) \rightarrow 2\ Ru^0\ (ss) + Te^0{}_2\ (g)$	6	840-1100
$Ce^{III}U^{V}O_4(ss) \rightarrow U^{IV}O_2(ss) + 1/2\ Ce^{III}{}_2O_3 + 1/4\ O_2(g)$	7	1270 -1300

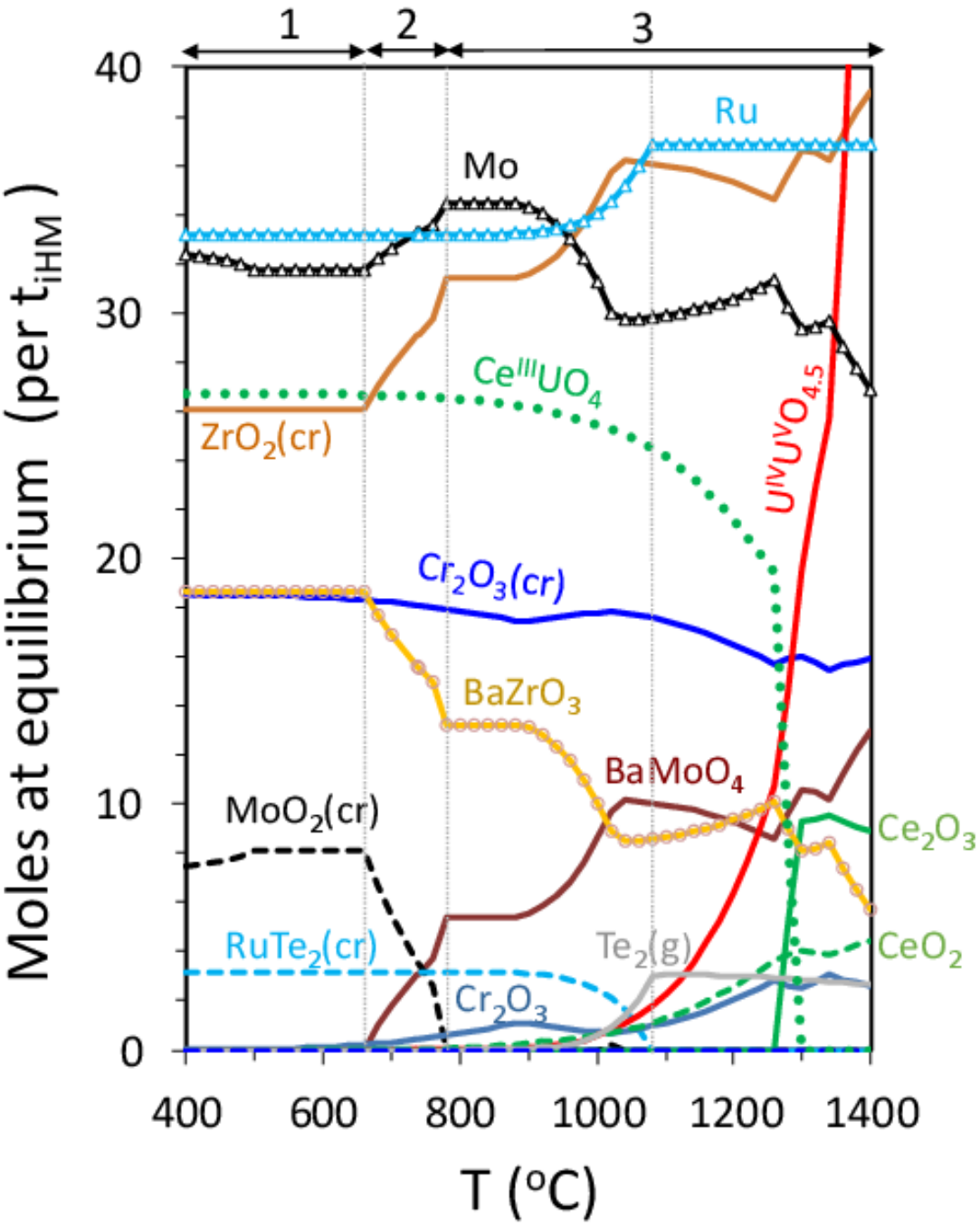

Fig. 6. Equilibrium amounts of stoichiometric solids, denoted by the suffix '(cr)', and solid solution end-members (without suffix) in one ton of initial Cr-doped fuel for the optimized '3 ss' model.

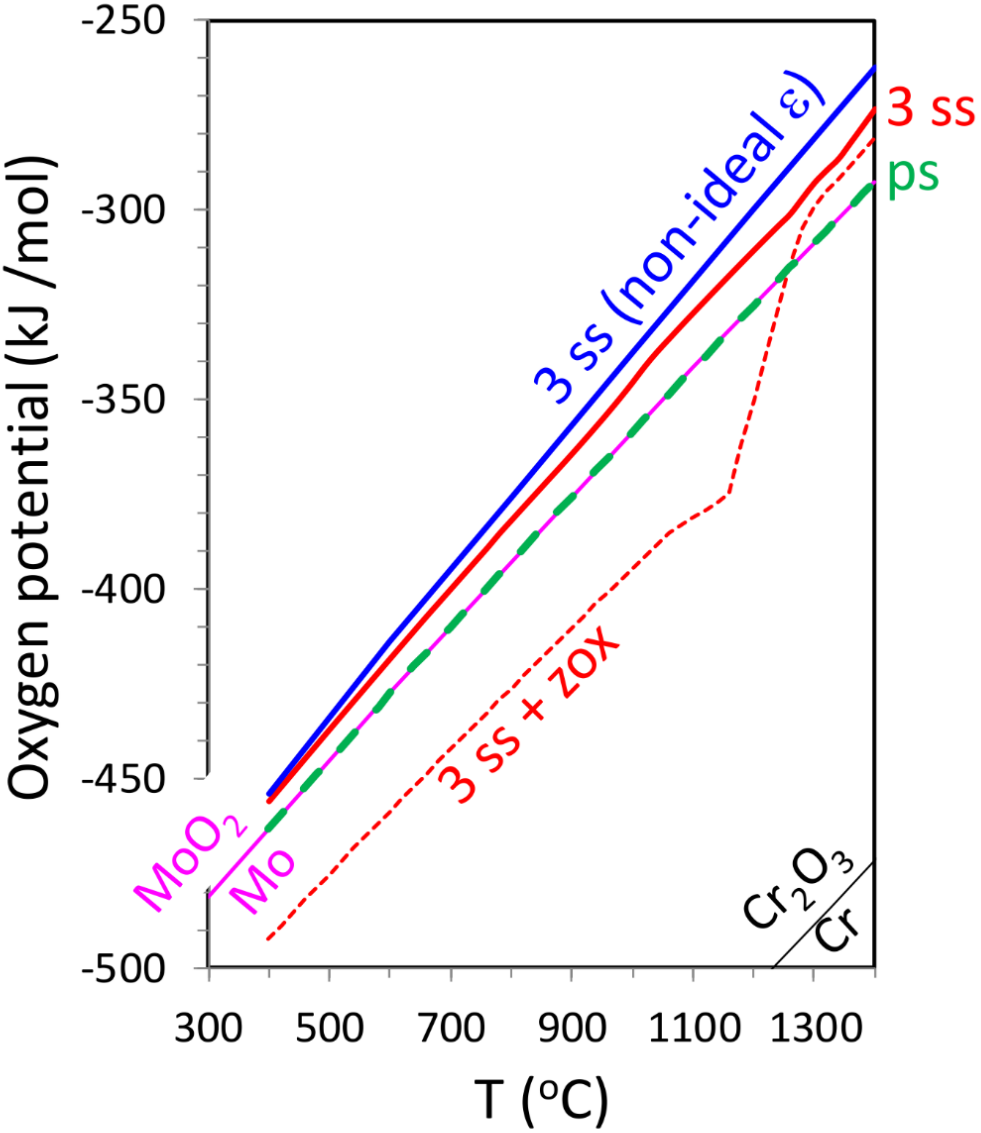

Fig. 7. Ellingham diagram including four distinct oxygen potential calculations for fuel inventory C (Table 2) and equilibrium lines for coexisting Mo-MoO_2 and Cr -Cr_2O_3 pure compounds.

Between 400 ºC and 1400 ºC, the speciation of chromium is dominated by Cr_2O_3(cr) (Fig. 6). Only a minor fraction remains as Cr_2O_3 solid solution component in the UO_2 phase. This is a consequence of the predicted segregation of chromium from the doped fuel at reactor operation temperatures, as evident from Fig. 8, where the calculated distribution of chromium

is shown from 1400 ºC up to fuel synthesis temperatures (1800-2000 ºC). At *T* = 1400 ºC the calculated solubility of Cr in urania is significant, but only about 15% of the Cr inventory is dissolved in the urania phase. Note that, since the oxygen potentials of the fuel are always well above the pure Cr - pure Cr_2O_3 buffer line, metallic chromium is never predicted to stable.

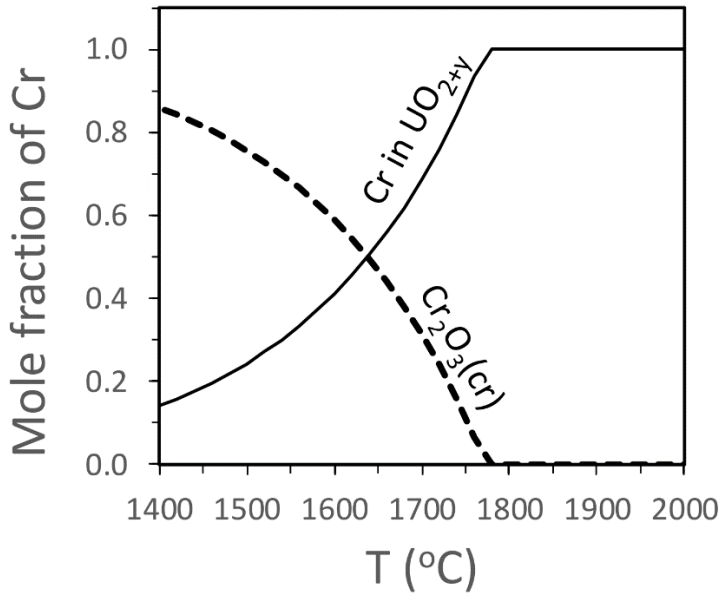

Fig. 8. Predicted chromium distribution at high temperatures for the optimized fuel model.

The calculated O/M ratios in the urania solid solution (where M includes U and all dissolved metals) are always very close to stoichiometry. They vary from 1.993 to 2.000 between 400 ºC and 1400 ºC, in agreement with the experimental findings of Matzke [65], who found O/M ratios in LWR irradiated fuels to range from slightly hypostoichiometric to barely hyperstoichiometric.

So far, the calculations related to the oxygen potential curve labeled '3 ss' in Fig. 7 were discussed . This corresponds to the optimized model set up in the preceding section for the Cr-doped fuel composition C, with the assumption of ideal mixing in the quinary ε-phase. An analogous calculation (not shown in Fig. 7) based on the equivalent non-doped fuel inventory

(composition A in Table 2) yielded an oxygen potential curve identical to the '3 ss' calculation. This result indicates that Cr-doping is not expected to affect the fuel oxygen potential, at least at the high burnup of 60 GWd/t_{iHM} to which the calculations refer. This is a major result of our study, indicating that no oxidation of fission products and fuel matrix should occur due to the presence of Cr-oxide dopant in the fuel.

The curve labeled 'ps' was computed neglecting formation of all three solid solutions defined in Section 3, i.e. also excluding the UO_2 solid solution. The calculations were thus carried out assuming that the fuel equilibrates only with stoichiometric phases listed in Table C3 (Appendix C). The results show coexistence of pure Mo metal and pure MoO_2 at all temperatures, therefore constraining the fuel oxygen potential exactly along the corresponding buffer line.

The curve labeled '3ss (non ideal ε)' differs from the '3ss' calculation only in the treatment of the noble metal phase. Instead of ideal mixing, non-ideality according to the model of Thompson et al. [41] was assumed for the quinary (Mo,Pd,Rh,Ru,Tc) solid solution. The effect of introducing non-ideality is a small, though significant, increase in oxygen potential from about 2 kJ/mol at 400 °C to 11 kJ/mol at 1400 °C. This effect can be understood by considering the following equations derived from the equilibrium expression of the reaction Mo(cr) + O_2(g) = MoO_2(cr):

$$p_{O_2} = \frac{1}{K\, a_{Mo}} \tag{4}$$

$$\Delta\bar{G}_{O_2} \cong RT \ln\left(p_{O_2}/p^o\right) = -RT(\ln K + \ln x_{Mo} + \ln \gamma_{Mo}) \tag{5}$$

where K is the temperature-specific equilibrium constant, R the gas constant, T is the absolute temperature and a_{Mo} , x_{Mo}, γ_{Mo} are the activity, mole fraction and activity coefficient of Mo in the noble metal phase.

The effect of non-ideality on the oxygen potential in a system where the noble metal solid solution coexists with pure MoO_2 is equal to $= -RT \ln \gamma_{Mo}$. This translates, for activity coefficients in the range 0.53-0.22, into $\Delta\bar{G}_{O_2}$ increase by 3-21 kJ/mol, compared to the calculation with ideal mixing ($\ln \gamma_{Mo} = 0$). Such an effect is indeed observed, see 'ss' and 'ss(on-ideal ε)'curves in Fig. 7, though the effect is mitigated by the destabilization of pure MoO_2 at T > 600 ^{o}C. Both curves lie above the pure Mo-MoO_2 buffer line, which is readily explained by the dilution effect ($x_{Mo} < 1$ leads to a positive $-RT \ln x_{Mo}$ term in eq. 5).

The fourth calculation in Fig. 7 (labeled '3 ss + zox') shows the effect of including internal zirconium alloy oxidation. This process was simulated in GEM-Selektor by adding in the input file an amount of reactive metallic Zr, corresponding to the formation of a 10 μm thick ZrO_2 layer at the inner side of the cladding. According to available experimental data [66, 67], this figure represents about the maximum observed corrosion depth. The results indicate that including zirconium alloy oxidation may lead to a considerable decrease in oxygen potential (by up to 40-60 kJ/mol) with respect to the corresponding calculation neglecting this effect ('3 ss'). Because zirconium alloy oxidation will occur at the internal cladding surface, the decrease in oxygen potential will mainly affect the rim of the fuel pellet and might be locally even larger than indicated by the calculation, which averages over the entire fuel pellet inventory. Thus, to some extent the zirconium alloy may buffer oxygen excess at the pellet-cladding interface, as recognized by Rondinella [68].

The changes in the slope of the '3 ss+ zox' curve could be explained by analyzing a plot (not shown) analogous to Fig. 6, indicating that oxidation of a 10 μm thick layer of zirconium alloy would be sufficient to destabilize $Mo^{IV}O_2$(cr) and $BaMo^{VI}O_4$(cr). Consequently, only metallic Mo is stable up to 1300 ^{o}C and therefore the pO_2 buffering reactions 1, 2, 3 (Table 3) are no longer active, determining low potentials up to 1150 ^{o}C. At T > 1150 ^{o}C the oxygen-producing reaction 7 becomes important. This reaction is related to the change in Ce

substitution mechanism from the (oxygen neutral) coupled substitution Ce^{III} + U^{V} for 2 U^{IV} to the substitution of 3 U^{IV} by 2 Ce^{III} (see Section 3.4), which requires formation of an oxygen vacancy and thus releases an equivalent amount of oxygen from UO_2. This explains the increased slope of the '3 ss+ zox' $\Delta\bar{G}_{O_2}$ curve between 1150 °C and 1300 °C. At this temperature, Ba molybdate becomes stable and reaction 3 controls pO_2 up to 1400 °C, recovering the original slope.

4.2 Evolution of oxygen potential with irradiation progress

The final set of calculations addresses the topic of oxygen potential evolution with increasing burnup. Calculations were carried out based on fuel model inventories at download time, derived from WebKOrigen++ [64] for burnups of 1, 23, 42, 53 and 60 GWd/t_{iHM}. These burnups correspond to 11 days and 1.2, 2.5, 3.6, 4.8 years of operation in a PWR, assuming in total five 292-days burning cycles and 73 days intervals for maintenance and reloading. The full thermodynamic model described in Section 3 was applied, with ideal mixing assumed for the noble metal phase.

The results (Fig. 9) indicate very low oxygen potentials in the initial stages of irradiation. With increasing burnup, they enter the regions defined by experimentally determined oxygen potentials and progressively increase up to values exceeding the pure Mo – pure MoO_2 buffer line. At 1 GWd/t_{iHM} the oxygen potentials of doped and non-doped fuel are almost identical up to 1180 °C, then the two curves diverge at higher temperatures: the potential of the non-doped fuel further decreases while the potential of the Cr-doped fuel increases exactly along the Cr-Cr_2O_3 buffer line. Inspection of the results shows that in the latter calculation, Cr(III) is partially reduced to metallic Cr at T ≥ 1180 °C. Therefore, since both Cr_2O_3 and Cr metal coexist at equilibrium, the fuel oxygen potential must follow the corresponding buffer line. At low temperatures (400 °C -700 °C) the oxygen potential is controlled by the O_2 consuming reaction Cs_2ZrO_3(cr) + Mo(ss) + 3/2 O_2(g) => ZrO_2(cr) + Cs_2MoO_4(cr). The shoulder between

800 ºC and 1060 ºC can be explained by the production of oxygen via decomposition of Cs molybdate (Cs_2MoO_4 => Mo_ss + 2 Cs(g) + 2 O_2(g)). The strong release of oxygen caused by this reaction is responsible for the increased slope increase between 800 ºC and 920 ºC. At this temperature the Cs molybdate is consumed, the O_2 release ceases and consequently the oxygen potential decreases.

At 23 GWd/t_{iHM} and up to 700 ºC the oxygen potential curves of doped and non-doped fuel coincide and are identical to those obtained at 1 GWd/t_{iHM} because of the previously mentioned buffering equilibrium among Cs_2ZrO_3(cr), Mo(ss), ZrO_2(cr) and Cs_2MoO_4(cr). Contrary to the calculation for 1 GWd/t_{iHM}, however, the amount of metallic molybdenum present in the fuel is now sufficient to avoid consumption of the Cs molybdate phase. Therefore, metallic Mo and Mo^{6+} coexist further at higher temperatures, preventing the decrease in oxygen potential predicted in the 1 GWd/t_{iHM} calculation.

The oxygen potentials computed for non-doped and Cr-doped fuel with burnups of 42 (not shown), 53 (not shown) and 60 GWd/t_{iHM} were found to coincide over the whole temperature range, exceeding the potentials of the pure Mo – pure MoO_2 buffer by about 5-20 kJ/mol. As previously discussed, this effect is a consequence of the dilution of Mo in the ε-particles solid solution. Test calculations (not shown) applying the RCM excess Gibbs energy functions indicate that this figure increases by additional 5-10 kJ/mol if the non-ideality of the quinary ε-particles solid solution is accounted for.

Finally, the oxygen potential curves depicted in Fig. 9 for 60 GWd/$_{tiHM}$ fuels (based on compositions B and D in Table 2) are found to be identical to the curves determined earlier for compositions A and B, which refer to spent fuel inventories calculated at two years after download. This result implies that oxygen potentials in irradiated LWR fuels should be rather insensitive to variations in fuel compositions induced by few years of decay. Therefore, the results presented in this study should be applicable to a large variety of irradiated LWR fuels.

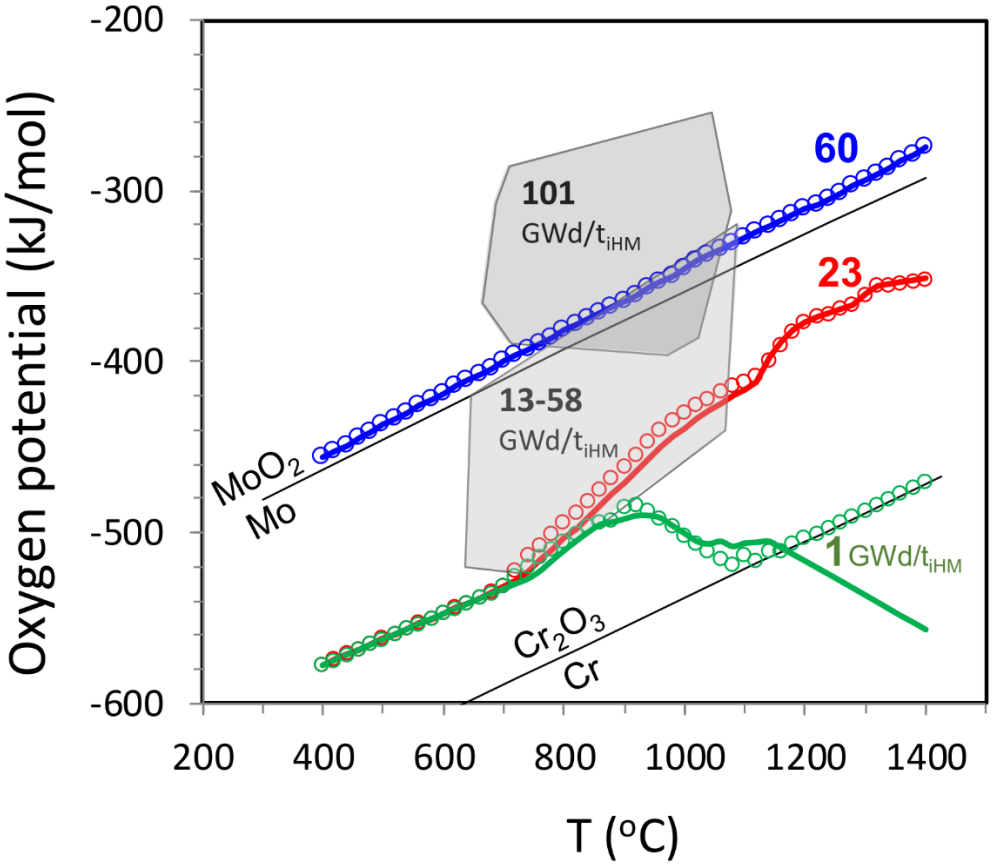

Fig. 9. Calculated evolution of oxygen potential for conventional and Cr-doped UO_2 fuel with increasing burnup. The grey fields delimit values of published experimental data for non-doped UO_2 fuels with burnups of 13-58 GWd/t_{iHM} [65, 69] and 101 GWd/t_{iHM} [70]. Colored lines indicate oxygen potentials for non-doped UO_2 fuel, calculated at the specified burnup. Circles show corresponding calculations for Cr-doped fuel. The oxygen potentials of Mo-MoO_2 and Cr-Cr_2O_3 pure metal/oxide pairs are shown as black lines.

Fig. 9 also shows the regions defined by experimental oxygen potential measurements on irradiated UO_2 fuels. The results of the calculations for fuels between 23 and 60 GWd/t_{iHM} overlap well the region defined by measurements on LWR fuel samples with burnup comprised between 13 and 58 GWd/t_{iHM}.

5. Summary and Conclusions

A comprehensive thermodynamic model was developed to predict chemical equilibria and oxygen potentials of Cr-doped and non-doped UO_2 fuels under operation conditions in light water reactors. The model includes three solid solution phases for urania, metallic inclusions (ε-particles) and a simplified 'grey phase'. The complex UO_2 phase takes into account the dissolution of Cr, Pu, minor actinides and rare earth fission products and was calibrated, as far as possible, with experimental data from the literature.

A critical step was the definition of thermodynamic properties and mixing parameters for trivalent REEs and actinides. The calibration procedure (carried out with the help of oxygen potential data for Nd and La-doped urania) showed that besides $Me^{III}_2O_3$ oxide component, end-members with stoichiometry $Me^{III}U^{V}O_4$ are compulsory to reproduce correctly oxygen potential data. These two end-members reflect distinct substitution mechanisms (incorporation of Me^{3+} in urania via oxygen vacancy formation or via charge compensation by U^{4+} to U^{5+} oxidation) in agreement with the findings of Ohmichi et al. [71] and Desgranges et al. [72].

The major conclusion from this modeling study is that Cr-doping should have no significant effect on the oxidation state of UO_2 fuels irradiated in light water reactors. Therefore, undesired effects such as increased fission gas release and enhanced diffusivity of radionuclides, or a reduction of thermal conductivity during neutron irradiation, are unlikely. As a result, enhanced segregation of volatile fission products (Cs, I) or oxidation of redox-sensitive radionuclides to water-soluble species is not expected to occur due to Cr-doping.

The comparison of solid solution model calculations with those obtained by simpler models in which only stoichiometric solids are equilibrated, reveals that the fuel oxygen potential is sensitive to the activity of Mo in the metallic inclusions. This leads to higher oxygen potentials with increasing dilution. The effect of non-ideal mixing, evaluated by

applying the model of Thompson et al. [41] is also significant, though very small (oxygen potential increase by < 11 kJ/mol). Surprisingly, replacing stoichiometric oxides with a complex non-ideal UO_2 solid solution has only a minor effect on the oxygen potential.

Calculations as a function of irradiation progress indicate low initial oxygen potentials of less than -500 kJ/mol (burnup 1 GWd/t_{iHM}), with significant differences between Cr-doped and non-doped fuel. At burnups exceeding about 20 GWd/t_{iHM} the calculated oxygen potentials overlap the region of experimentally determined oxygen potentials and only minor differences between Cr-doped and non-doped fuel are computed. At higher burnups (≥ 42 GWd/t_{iHM}) the calculated oxygen potentials of Cr-doped and non-doped fuels are identical and converge to values about 5-20 kJ/mol above the line defined by the pure Mo-MoO_2 buffer. Finally, calculations carried out to estimate the effect of zirconium alloy oxidation at the internal side of the cladding, indicate that this process may considerably reduce the oxygen potential (by 40-60 kJ/mol).

Data availability

Part of the data required to reproduce the findings presented in this publication are provided in Appendix B, C, D and E in this document. Additional data can be retrieved from the internet sources indicated in Appendix A. Input files and results of all calculations can be obtained by explicit request to the corresponding author.

Acknowledgments

This project has received funding from the European Union's Horizon 2020 research and innovation programme under grant agreement No 755443 — DISCO — NFRP-2016-2017/NFRP-2016-2017-1. Additional financial support was provided by Swiss National Cooperative for the Disposal of Radioactive Waste (Nagra). Dr. G.D. Miron is kindly acknowledged for his help with the application of the GEMSFIT software.

Appendix A. Code and thermodynamic database

All calculations described in this contribution have been carried out using version 3.4.2 of GEM-Selektor code [11, 12] and our in-house thermodynamic database (HERACLES). GEM-Selektor can be downloaded free of charge at http://gems.web.psi.ch/, along with documentation and tutorials. The HERACLES database is a compilation of thermodynamic data aiming at supporting modeling of nuclear materials over a wide range of compositions and temperatures. It includes molar thermodynamic properties of solid compounds of uranium, plutonium, minor actinides, fission products and auxiliary data taken from different published sources. At present, data for over 610 condensed compounds (including melts and liquid condensates) and over 360 gaseous species are provided. A downloadable GEM-Selektor specific version is available at https://www.psi.ch/en/heracles. Thermodynamic properties and their sources can be inspected individually in GEM-Selektor's database mode.

Appendix B. Thermodynamic data for chromium

Chromium is not included in the current HERACLES database. Therefore, a selection of Cr data relevant to this study had to be implemented. All data were taken from the comprehensive compilation of Barin [73], after verifying that the reported Gibbs energies are consistent with those given in primary references [74, 75]. In order to include heat capacities in GEM-Selektor, Barin's tabulated data were interpolated to obtain the coefficients for the following 10-term equation, which is used in the GEM-Selektor code for temperature extrapolation:

$$c_p(T) = a_0 + a_1T + a_2T^{-1} + a_3T^{-0.5} + a_4T^2 + a_5T^3 + a_6T^4 + a_7T^{-3} + a_8T^{-1} + a_9T^{-0.5}$$

Tables B1 and B2 list the selected data (molar Gibbs free energy of formation and molar entropy at 298.15 K, 1 bar; heat capacity coefficients).

Table B1. Selected thermodynamic data for chromium solids.

Property	Cr_2O_3	Cr	CrO_2	CrO_3	CrI_2	CrI_3
$\Delta_f G^0$ (kJ mol^{-1})	-1057.9	0	-544.84	-512.51	-165.56	-205.47
S^0 (J mol^{-1} K^{-1})	81.199	23.64	51.045	73.22	169.034	199.577
c_p^0 (J mol^{-1} K^{-1})	117.563	23.2385	99.6717	69.326	73.679	111.675
a_0	118.3	32.3349	94.5583	82.5486	66.9438	105.437
a_1	0.0099	-0.01589	0.01715	0.02168	0.02259	0
a_2	-1.4×10^6	-542904	13.2353	-1.75×10^6	0	0
a_3	0	0	0	0	0	0
a_4	0	2.1×10^{-5}	0	0	0	0
a_5	0	-4.46×10^{-9}	0	0	0	0
a_6	0	0	0	0	0	0
a_7	0	0	0	0	0	0
a_8	0	0	0	0	0	0
a_9	0	0	0	0	0	0

Table B2. Selected thermodynamic data for chromium gas species.

Property	Cr(g)	CrO(g)	CrO_2(g)	CrO_3(g)
$\Delta_f G^0$ (kJ mol^{-1})	352.62	154.63	-87.311	
S^0 (J mol^{-1} K^{-1})	174.306	239.267	269.224	
c_p^0 (J mol^{-1} K^{-1})	20.7901	31.3316	43.3263	
a_0	21581.2	64.228	40.5625	66.7745
a_1	6.68684	0.00784	0.03006	0.02175
a_2	-2.45743×10^8	-1.67675×10^6	-413342	-1.48×10^6
a_3	-442123	-569.757	0	0
a_4	-6.77344×10^{-4}	-6.62987×10^{-7}	-1.86×10^{-5}	-1×10^{-5}
a_5	7.65224×10^{-8}	7.75564×10^{-11}	3.95×10^{-9}	1.52×10^{-9}
a_6	-4.62271×10^{-12}	-4.25608×10^{-15}	0	0
a_7	1.21458×10^{10}	2.4525×10^8	0	0
a_8	4.18341×10^6	5621.34	0	0
a_9	-556.889	-0.66168	0	0

Appendix C. List of condensed phases and gaseous species

Tables C1 to C3 list phases and gaseous species included in the thermodynamic treatment presented in this study.

Table C1. Complete list of all solid phases considered for equilibration in the present study. The phases that were found to be stable in at least one calculation at any temperature between 400 ºC and 1400 ºC are highlighted in bold face.

Solid solutions (not part of HERACLES database)			
Phase name		Phase name	Phase name
UCrPuREE_mAn_fin		**BaSr-ZrO3_ISS**	**MoPdRhRuTc_ISS**
End-members		End-members	End-members
$(NpO_2)_2$	Ce_2O_3	$BaZrO_3$	Mo
$(NpO_{2.5})_2$	$Cm^{III}U^{V}O_4$	$SrZrO_3$	Pd
Am_2O_3	Cr_2O_3		Rh
Cm_2O_3	$La^{III}U^{V}O_4$		Ru
$(CeO_2)_2$	La_2O_3		Tc
$(PuO_2)_2$	$Nd^{III}U^{V}O_4$		
$(U_2O_{4.5})$	Nd_2O_3		
$(UO_2)_2$	$Pu^{III}U^{V}O4$		
$Am^{III}U^{V}O_4$	Pu_2O_3		
$Ce^{III}U^{V}O_4$			

Stoichiometric solid phases (HERACLES database and newly defined Cr phases)			
Am	CsO_2	**NpO_2**	$SrSeO_3$
Am_2O_3	Cs_2SeO_4	$NpO_{2.5}$	SrTe
Ba	Cs_2Te	**Pd**	$Sr_3U_2O_9$
BaI_2	Cs_2Te2O_5	Pd_4Se	$SrUO_4$
$BaMoO_4$	$Cs_2Te_4O_{12}$	PdTe	**$SrZrO_3$**
BaO	$Cs_2Te_4O_9$	Pu	**Tc**
BaSe	Cs_2TeO_3	PuI_3	Te
$BaSeO_3$	Cs_2TeO_4	Pu_2O_3	TeO_2
$BaSeO_4$	$Cs_2U_2O_7$	$PuO_{1.16}$	U
$BaZrO_3$	$Cs_2U_4O_{12}$	$PuO_{1.5}$	UI_3
BaTe	Cs_2UO_4	**PuO_2**	UI_4
BaTe	$Cs_4U_5O_{17}$	PuOI	U_3O_8
$BaUO_4$	Cs_2ZrO_3	PuSe	U_4O_9
Ce	I_2	Rb	UO_2
$CeCrO_3$	La	**RbI**	$UO_{2.25}$
CeI_3	LaI_3	**Rb_2O**	$UO_{2.5}$
Ce_2O_3	**La_2O_3**	RbO_2	UO_3
CeO_2	La_2Se_3	Rb_2SeO_4	UO_2SeO_3
Cm	LaSe	**Rh**	UO_2SeO_4
Cm_2O_3	La_2Te_3	Rh_2O	U_3Se_4
CmO_2	LaTe	Rh_2O_3	USe
Cr	**Mo**	**Ru**	USe_2
Cr_2O_3	MoI_2	RuO_2	Zr
CrI_2	MoI_3	PdO	ZrI
CrI_3	MoI_4	**$RuSe_2$**	ZrI_2
CrO_2	**MoO_2**	**$RuTe_2$**	ZrI_3
CrO_3	MoO_3	Se	ZrI_4
Cs	Nd	SeO_2	ZrO
CsI	**Nd_2O_3**	SeO_3	**ZrO_2**
Cs_2MoO_4	Np	Sr-β	$ZrTe_2$
Cs_2O	NpI_3	SrI_2	
Cs_2O_2	Np_2O_5	SrO	

Table C2. Complete list of liquid phases considered for equilibration in the present study. The phases found to be stable in at least one calculation at any temperature between 400 ºC and 1400 ºC are highlighted in bold face. No mutual miscibility was assumed.

Am(l)	Cr_2O_3(l)	Nd(l)	Th(l)
Ba(l)	Cs(l)	Pu(l)	ThO(l)
BaI2(l)	CsI(l)	**RbI(l)**	U(l)
BaO(l)	CsOH(l)	Rb_2O(l)	UO_2(l)
CSe_2(l)	I_2(l)	RbO_2(l)	Zr(l)
Ce(l)	LaI_3(l)	Se(l)	ZrI_2(l)
CeI3(l)	La_2O_3(l)	Sr(l)	ZrO_2(l)
Cm(l)	Mo(l)	SrI_2(l)	
Cr(l)	MoO_3(l)	SrO(l)	

Table C3. Complete list of gaseous species considered for equilibration in the present study. In all calculations ideal mixing and a total pressure of 1 bar were assumed.

Am(g)	CsO(g)	Nd(g)	SrI(g)
Ar(g)	CsRb(g)	NdO(g)	SrI_2(g)
Ba(g)	I(g)	NdO_2(g)	Te(g)
Ba2(g)	I_2(g)	Np(g)	Te_2(g)
Ba_2O(g)	IO(g)	O(g)	Te_2O_2(g)
Ba_2O_2(g)	IO_3(g)	O_2(g)	TeO(g)
BaI(g)	Kr(g)	O_3(g)	TeO_2(g)
BaI_2(g)	La(g)	Pu(g)	U(g)
$BaMoO_4$(g)	La_2O(g)	PuI_3(g)	UI(g)
BaO(g)	La_2O_2(g)	PuO(g)	UI_2(g)
Ce(g)	LaI3(g)	Rb(g)	UI_3(g)
CeI_3(g)	LaO(g)	Rb_2(g)	UI_4(g)
CeSe(g)	LaSe(g)	RbI(g)	UO(g)
CeTe(g)	LaTe(g)	Se(g)	UO_2(g)
Cm(g)	Mo(g)	Se_2(g)	UO_3(g)
Cr(g)	Mo_2O_6(g)	Se_3(g)	USe(g)
CrO(g)	Mo_3O_9(g)	Se_4(g)	Xe(g)
CrO_2(g)	Mo_4O_{12}(g)	Se_5(g)	Zr(g)
CrO_3(g)	Mo_5O_{15}(g)	Se_6(g)	ZrH(g)
Cs(g)	MoI(g)	Se_7(g)	ZrI(g)
Cs_2(g)	MoI_2(g)	Se_8(g)	ZrI_2(g)
Cs_2I_2(g)	MoI_3(g)	SeO(g)	ZrI_3(g)
Cs_2MoO_4(g)	MoI_4(g)	SeO_2(g)	ZrI_4(g)
Cs_2O(g)	MoO(g)	SeTe(g)	ZrO(g)
Cs_2O_2(g)	MoO_2(g)	Sr(g)	ZrO_2(g)
CsI(g)	MoO_3(g)	Sr_2(g)	

Appendix D. Sublattice Berman model as implemented in GEM-Selektor v.3.4 code

The treatment of non-electrolyte solid solutions in GEM-Selektor is based on the following expression for the reduced (dimensionless) chemical potential $\upsilon_j \equiv \mu_j/(RT)$ of a j-th end-member:

$$\upsilon_j = \frac{g_{j,T,P}}{RT} + \ln x_j + \ln f_j \qquad \text{(D1)}$$

where μ_j and $g_{j,T,P}$ are the chemical potential and the molar Gibbs free energy at T, P of interest; x_j is the end-member mole fraction and f_j is a 'real' activity coefficient. If all activity coefficients are equal to 1, then eq. D1 reduces to Raoult's law and activities equal mole fractions. This reference definition of ideal mixing, corresponding to the configurational entropy resulting from random one-to-one mixing of species on a single type of structural sites, is restrictive and cannot be directly applied to sublattice solid solutions, where moieties (ions, atoms, molecules) can substitute for each other independently on several sites, often called 'sublattices' (i.e. sets of structurally identical sites).

Eq. D1 corresponds to the simplest case where a set of species (two or more moieties) substitute for each other on a single sublattice. This approach is insufficient for complex solid solutions like $(U,Cr,Ln,An)_{1\pm x}O_{2\pm y}$, in which mixing occurs on several sublattices simultaneously. In multisite *ideal* solid solutions, the activity a_j of a given species j is not simply equal to the mole fraction x_j, but is a complex function of 'site fractions' $y_{s,m}$, where the index m denotes a specific substituting species and the index s a specific site. This leads to a generalized form of the configurational entropy and to *'reciprocal' relations* between end-members and their standard-state properties ([31, 34]). Accordingly, the generalized form of eq. D1 is:

$$\upsilon_j = \frac{g_{j,T,P}}{RT} + \ln a_j^{(con)} + \ln f_j \qquad \text{(D2)}$$

where f_j is the 'macroscopic' end-member activity coefficient, and $a_j^{(con)}$ is the ideal part of activity related to the partial molar configurational entropy. Application of this model leads to the following expression for the configurational entropy part of the activity (a complete demonstration is available in the documentation files supplied with the GEM-Selektor code):

$$a_j^{(con)} = \prod_s \prod_m \left(y_{s,m} \frac{\eta_s}{\eta_{j,s,m}} \right)^{\eta_{j,s,m}} \qquad \text{(D3)}$$

where η_s is the "site multiplicity", i.e. the stoichiometric factor of the *s*-th site in the formula of any end-member *j*, and $\eta_{j,s,m}$ is the "moiety-site multiplicity", i.e. the stoichiometric factor of the *m*-th moiety in the *s*-th site of end-member *j*. For example, given a three-sites solid solution with composition $^{I}\{A_{0.2}, B_{0.3}, C_{0.5}\}_2\ ^{II}\{X_{0.1}, Y_{0.7}, Z_{0.2}\}_3\ ^{III}\{O\}_5$ in which the species A, B, C mix within site I and X, Y, Z mix within site II and no mixing occurs in site III, the site multiplicities are 2, 3 and 5 for site I,II and III, respectively. The moiety-site multiplicities of species B in end-members $B_2X_3O_5$, $A_2X_3O_5$ and $B_2Z_3O_5$ in the first site are 2, 0, 2, respectively.

To represent intra-site non-ideal interactions for substitutions in the three sublattices of UO_2, the model of Berman [27, 28] was applied, according to which the non-ideal contribution to the activity end-member *j* (see eq. D2) is defined by the following two equations:

$$\ln f_j = \sum_s \sum_m \ln \gamma_{j,s,m} \qquad \text{(D4)}$$

$$\ln \gamma_{j,s,m} = \frac{\eta_{j,s,m}}{\eta_s RT} \sum_t \left[y_d\, y_e\, y_f\, W_{def,s} \left(\frac{\eta_{j,s,m}}{\eta_s} \frac{Q_{s,m}}{y_{s,m}} - \Theta \right) \right] \qquad \text{(D5)}$$

where the index m refers only to moieties that are present in a specific s-site in the j-th end member; $Q_{s,m}$ is the number of $_d$, $_e$, $_f$ subscripts equal to m (0, 1 or 2); Θ is the order of interaction (symmetric: 1; asymmetric: 2). The $_d$, $_e$, or $_f$ subscripts correspond to the index m of any moiety that exists on the s-th site. Temperature and pressure dependence of the interaction coefficients $W_{def,s}$ is calculated with the following equation using the 3 coefficients a, b, c:

$$W_{def,s} = a - b \cdot T + c \cdot P \qquad \text{(D6)}$$

In this study, T,P-independent interaction coefficients were used, so that eq. D6 simplifies to:

$$W_{def,s} = a \qquad \text{(D7)}$$

An example of how the Berman-type solid solution was implemented in GEM-Selektor is shown in Tables D1 to D3 for the ternary, 3-sites $(U,Cr)O_{2+y}$ solid solution defined in this study. These Tables are identical to those effectively appearing in the "Phase definition" module of GEM-Selektor, except for the explanatory text in italics. Table D1 shows how the site and element stoichiometry is implemented. Note that vacancies are treated explicitly (symbol 'Va') and distinct moieties must be defined for the same element (or vacancy) if they belong to different sites. For instance, {O}1 and {O}2 in the second row of Table D2 refer to O^{2-} anions in the anionic and interstitial sublattice, respectively. If no oxidation state is specified by vertical bars (Table D1), then the default oxidation state is assumed (-II in the case of oxygen). The meaning of the various indices and coefficients are shown in the heading rows of Table D2 and D3.

Table D1. Definition of Berman-type $(U,Cr)O_{2+y}$ solid solution in GEM-Selektor: (A) definition of end-member stoichiometries and sites. Each moiety (species) is enclosed in braces. Explicit oxidation states are delimited by vertical bars. Sites are separated by colons.

Name of end-member	*GEM-Selektor formula*	*end-member index, j*
(U2O4.5)_ss	{U|5|}{U|4|}:{O}4:{Va}1.5{O}0.5:	*j = 0*
(UO2)2_ss	{U|4|}2:{O}4:{Va}2:	*j = 1*
Cr2O3_ss	{Cr|3|}2:{O}3{Va}1:{Va}2:	*j = 2*

Table D2. Definition of Berman-type $(U,Cr)O_{2+y}$ solid solution in GEM-Selektor: (B) Definition of end-member. The number outside the braces in the second row denote the site (0, 1 or 2) to which the moiety belongs (i.e. it corresponds to index '*s*'). The numbers in the Table are stoichiometric coefficients assigned to the 7 moieties (*m*=0...6) for each of the three end-members considered. Zero values imply that the specific moiety is absent in a given end-member.

m = 0	*m = 1*	*m = 2*	*m = 3*	*m = 4*	*m = 5*	*m = 6*	*<= moiety index, m*
{U|5|}0	{U|4|}0	{O}1	{Va}2	{O}2	{Cr|3|}0	{Va}1	*name of end-member:*
1	1	4	1.5	0.5	0	0	(U2O4.5)_ss
0	2	4	2	0	0	0	(UO2)2_ss
0	0	3	2	0	2	1	Cr2O3_ss

Table D3. Definition of Berman-type $(U,Cr)O_{2+y}$ solid solution in GEM-Selektor: (C) Table defining interaction coefficients $W_{def,s}$. The first row identifies indices and coefficients appearing in eqs. Numbers below column *s* identify sites or sublattices (0=cationic, 1=anionic, 2= interstitial). Numbers below columns *d, e, f* identify the moieties, i.e. they correspond to the *m*-values indicated in Table D2. Numbers below columns *a,b,c* specify the values assigned to the coefficients of eq. (D5).

index/coefficient=>	*s*	*d*	*e*	*f*	*a*	*b*	*c*
W_Cr_Cr_U4	0	5	5	1	0	0	0
W_Cr_Cr_U5	0	5	5	0	0	0	0
W_Cr_U4_U4	0	5	1	1	255000	0	0
W_Cr_U5_U5	0	5	0	0	0	0	0
W_U4_U5_U5	0	1	0	0	100000	0	0
W_U4_U4_U5	0	1	1	0	100000	0	0
W_Cr_U4_U5	0	5	1	0	0	0	0
W_O1_O1_Va1	1	2	2	6	0	0	0
W_O1_Va1_Va1	1	2	6	6	0	0	0
W_Va2_Va2_O2	2	3	3	4	0	0	0
W_Va2_O2_O2	2	3	4	4	0	0	0

Appendix E. Implementation of RCM noble metal solid solution model

The first step was to calculate the partial derivatives of the excess Gibbs energy function given in the RCM database for the hexagonal close packed (hcp) quinary noble metal solid solution [41]. The following expressions were obtained:

$$\frac{\partial G_{ex}}{\partial x_{Mo}} = (-8453.15 - 5.495\ \mathrm{T})x_{Mo} + 20920x_{Pd} + (10\ \mathrm{T} - 89730)x_{Mo}x_{Pd} + 2\,(25.872\ \mathrm{T} - 60006.5)x_{Mo}x_{Rh} + (10.455\ \mathrm{T} - 26440)x_{Ru} - 90000x_{Ru}x_{Pd} + (21.28\ \mathrm{T} - 28250)x_{Tc} + (-111959 + 28.94\ \mathrm{T})x_{Tc}^2 \quad \text{(E1)}$$

$$\frac{\partial G_{ex}}{\partial x_{Tc}} = (59650 - 20\ \mathrm{T})x_{Mo} - (5962.7 + 12.92\ \mathrm{T})x_{Pd} + (21.28\ \mathrm{T} - 28250)x_{Rh} + 2\,(27437 - 10\ \mathrm{T})x_{Mo}x_{Tc} + 2\,(4296 + 27.13\ \mathrm{T})x_{Pd}x_{Tc} + 2\,(28.94\ \mathrm{T} - 111959)x_{Rh}x_{Tc} \quad \text{(E2)}$$

$$\frac{\partial G_{ex}}{\partial x_{Pd}} = (11387 - 16.81\ \mathrm{T})x_{Mo} + 2\,(656.46 - 53.33\ \mathrm{T})x_{Mo}x_{Pd} + 20920\,x_{Rh} + (10\ \mathrm{T} - 89730)x_{Mo}x_{Rh} + (14.933\ \mathrm{T} - 1524.82)x_{Ru} - 15000x_{Mo}x_{Ru} - 130000x_{Mo}^2x_{Ru} - 90000x_{Rh}x_{Ru} - (5962.7 + 12.92\ \mathrm{T})x_{Tc} + (4296 + 27.13\ \mathrm{T})x_{Tc}^2 \quad \text{(E3)}$$

$$\frac{\partial G_{ex}}{\partial x_{Ru}} = (78174 - 50\ \mathrm{T})x_{Mo} + (14.933\ \mathrm{T} - 1524.82)x_{Pd} - 15000x_{Mo}x_{Pd} - 130000\,x_{Mo}^2x_{Pd} + (10.455\ \mathrm{T} - 26440)x_{Rh} - 90000x_{Pd}x_{Rh} + 2\,(80\ \mathrm{T} - 169180)x_{Mo}x_{Ru} \quad \text{(E4)}$$

$$\frac{\partial G_{ex}}{\partial x_{Rh}} = 20920x_{Pd} - (8453.15 + 5.495\ \mathrm{T})x_{Mo} + +(10\ \mathrm{T} - 89730)x_{Mo}x_{Pd} + (25.872\ \mathrm{T} - 60006.5)x_{Mo}x_{Rh} + x_{Ru}(10.455\ \mathrm{T} - 26440) - 90000\,x_{Pd}x_{Ru} + (21.28\ \mathrm{T} - 28250)x_{Tc} + (28.94\ \mathrm{T} - 111959)x_{Tc}^2 \quad \text{(E5)}$$

The activity coefficients γ_i were then derived from eq. E1-E5 through the relation:

$$\frac{\partial G_{ex}}{\partial x_{Ru}} = R\,\mathrm{T}\ln\gamma_i \quad \text{(E6)}$$

For a typical ε-particle composition (x_{Mo}=0.30, x_{Tc}=0.11, x_{Pd}=0.23, x_{Ru}=0.30, x_{Rh}=0.055) as determined by the calculations carried out using the *ideal* mixing model, the activity coefficients resulting from the *non-ideal* RCM model as a function of temperature, are shown

in Fig. E1. These activity coefficients were selected as initial guesses for GEM-Selektor calculations, in which non-ideality was assumed (represented as Berman model with 6 binary and 3 ternary interaction coefficients, see Fig. E2) .

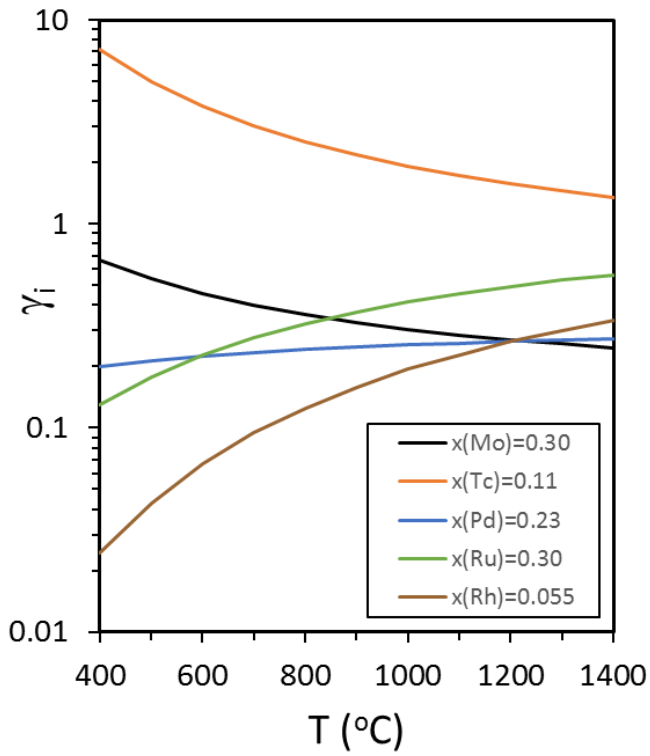

Fig. E1. Activity coefficients calculated from the RCM model for the indicated ε-particle composition.

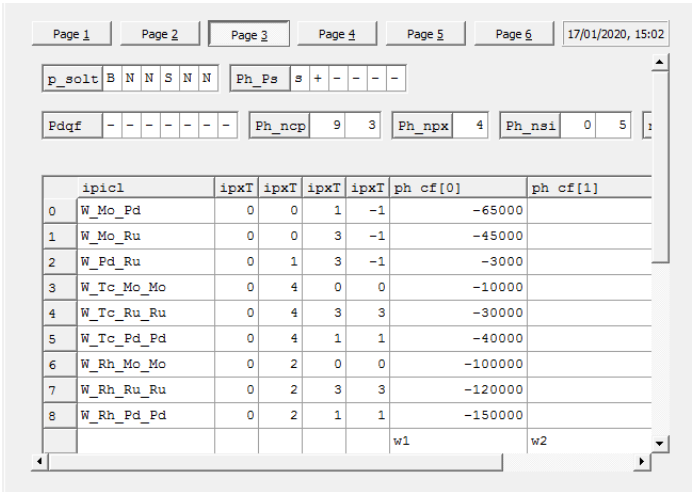

Page 1 | Page 2 | Page 3 | Page 4 | Page 5 | Page 6 | 17/01/2020, 15:02

p_solt B N N S N N | Ph_Ps s + - - - -

Pdqf - - - - - - - | Ph_ncp 9 3 | Ph_npx 4 | Ph_nsi 0 5

	ipicl	ipxT	ipxT	ipxT	ipxT	ph cf[0]	ph cf[1]
0	W_Mo_Pd	0	0	1	-1	-65000	
1	W_Mo_Ru	0	0	3	-1	-45000	
2	W_Pd_Ru	0	1	3	-1	-3000	
3	W_Tc_Mo_Mo	0	4	0	0	-10000	
4	W_Tc_Ru_Ru	0	4	3	3	-30000	
5	W_Tc_Pd_Pd	0	4	1	1	-40000	
6	W_Rh_Mo_Mo	0	2	0	0	-100000	
7	W_Rh_Ru_Ru	0	2	3	3	-120000	
8	W_Rh_Pd_Pd	0	2	1	1	-150000	
						w1	w2

Fig. E2. GEM-Selektor window specifying the interaction coefficients for the non-ideal ε-particle solid solution. This selection of coefficients provides sufficient flexibility to perform successfully the optimization procedure described in the text.

GEM-Selektor computations corresponding to the '3ss' curve shown in Fig. 7 were then carried out at 400, 600, 800, 1000, 1200 and 1400 ^{o}C. The values of the interaction coefficients were varied by trial and error until the target activity coefficients (first guesses) were obtained with reasonable precision at a given temperature. The resulting ε-particle composition was checked and in case of significant deviations from the initial composition, the aforementioned procedure was iterated until convergence was reached. However deviations from the initial composition were in general so small, that virtually no iteration was needed. Such more or less constant composition of ε-particles was expected, since Rh, Pd and Tc are stable only in the metallic form at the oxygen potentials of interest and the amounts of Mo and Ru residing in other phases (MoO_2, $CsMoO_4$, $RuSe_2$, $RuTe_2$) are always much smaller than the inventories in the ε-phase. Table E1 reports the values of fitted activity coefficients.

Table E1. Fitted activity coefficients for '3ss' calculations

T(^{o}C)	γ_{Mo}	γ_{Tc}	γ_{Pd}	γ_{Ru}	γ_{Rh}
400	0.658	6.781	0.207	0.131	0.024
600	0.446	3.536	0.238	0.233	0.067
800	0.365	2.631	0.234	0.319	0.125
1000	0.293	1.819	0.280	0.424	0.195
1200	0.254	1.469	0.321	0.511	0.267
1400	0.222	1.213	0.375	0.638	0.348

It is instructive to inspect the values of molybdenum activity coefficients. The values of γ_{Mo} vary from 0.658 at 400 ^{o}C and decrease continuously to 0.222 at 1400 ^{o}C. According to eq. 5 this corresponds to an increase in oxygen potential from about 3 kJ/mol (40 ^{o}C) to 21 kJ/mol (1400 ^{o}C) with respect to the ideal solid solution, as long as the ε-phase coexists with MoO_2. In the full calculations a similar trend is observed, but the differences are smaller (from 2.3 to 11 kJ/mol), because from 600 ^{o}C upwards MoO_2 is no longer stable.

References

[1] J. Arborelius, K. Backman, L. Hallstadius, M. Limbäck, J. Nilsson, B. Rebensdorff, G. Zhou, K. Kitano, R. Löfström, G. Rönnberg, Advanced Doped UO_2 Pellets in LWR Applications, J. Nucl. Sci. Technol. 43(9) (2006) 967–976.

[2] C. Nonon, J.-C. Menard , S. Lansiart, et al., PCI behaviour of chromium oxide-doped fuel, in: Pellet–clad interaction in water reactor fuels, Seminar Proceedings, March 9–11, 2004, Aix-en-Provence, France, Organisation for Economic Co-Operation and Development, Nuclear Energy Agency, NEA No. 6004, 2005, pp. 305–320.

[3] M.H.A. Piro, D. Sunderland, S. Livingstone, J. Sercombe, W. Revie, A. Quastel, K. Terrani, C. Judge, A Review of Pellet–Clad Interaction Behavior in Zirconium Alloy Fuel Cladding, in: Saleen Hashmi (Ed.), Reference Module in Materials Science and Materials Engineering, Elsevier Oxford, 2017, pp. 1–68.

[4] L.Z. Evins, L. Duro, A. Valls, C. Corkhill, E. Myllykylä, I. Farnan, D. Bosbach, V. Metz, P. Maldonado, Spent nuclear fuel dissolution (REDUPP and DISCO) Programme and Abstracts, EURADWASTE'19, 9th European Commission Conference on EURATOM Research and Training in Radioactive Waste Management, 4-7 June, 2019, Pitesti, Romania, ISBN 978-92-79-98743-4.

[5] D.R. Olander, Fundamental aspects of nuclear reactor fuel elements, National Technical Information Service, U.S. Dept. of commerce, Springfield (VI), U.S.,1976.

[6] P.G. Lucuta, Hj. Matzke, R.A. Verrall, Thermal conductivity of hyperstoichiometric SIMFUEL, J. Nucl. Mater. 223 (1995) 51–60.

[7] P. Carbol, P. Fors, Th. Gouder, K. Spahiu, Hydrogen suppresses UO_2 corrosion, Geochim. Cosmochim. Acta 73 (2009) 4366–4375.

[8] Y. Kumagai, A. Barreiro Fidalgo, M. Jonsson, Impact of stoichiometry on the mechanism and kinetics of oxidative dissolution of UO_2 induced by H_2O_2 and γ-irradiation, J. Phys. Chem. C 123 (2019) 9919−9925.

[9] M.S. Veshchunov, R. Dubourg, V.D. Ozrin, V.E. Shestak, V.I. Tarasov, Mechanistic modelling of urania fuel evolution and fission product migration during irradiation and heating, J. Nucl. Mater. 362 (2007) 327–335.

[10] Ozrin V.D., A model for evolution of oxygen potential and stoichiometry deviation in irradiated UO_2 fuel, J. Nucl. Mater. 419 (2011) 371–377.

[11] Th. Wagner, D.A. Kulik, F.F. Hingerl, S.V. Dmytrieva, GEM-Selektor geochemical modeling package: TSolMod library and data interface for multicomponent phase models, Can. Mineral. 50 (2012) 1173–1195.

[12] D.A. Kulik, Th. Wagner, S.V. Dmytrieva, G. Kosakowski, F.F. Hingerl, K.V. Chudnenko, U. Berner, GEM-Selektor geochemical modeling package: Revised algorithm and GEMS3K numerical kernel for coupled simulation codes, Computat. Geosci. 17 (2013) 1–24.

[13] GEMS specific HERACLES v.0.2. database for U, TRU and FP speciation, https://www.psi.ch/en/heracles/gems-specific-heracles-database (accessed 30 January 2020).

[14] B.T.M. Willis, Structures of UO_2, UO_{2+x} and U_4O_9 by neutron diffraction, Journal de Physique 25 (1964) 431–439.

[15] J. Yu, X.-M. Bai, A. El-Azab, T.R. Allen, Oxygen transport in off-stoichiometric uranium dioxide mediated by defect clustering dynamics, J. Chem. Phys. 142 (2015) 094705.

[16] D. Prieur, Ph. Martin, F. Lebreton, Th. Delahaye, D. Banerjee, A.C. Scheinost, A. Jankowiak, Accommodation of multivalent cations in fluorite-type solid solutions: Case of Am-bearing UO_2, J. Nucl. Mater. 434 (2013) 7–16.

[17] J. Wang, R.C. Ewing , U. Becker, Average structure and local configuration of excess oxygen in UO_{2+x} , Scientific Reports (2014) 4:4216.

[18] D. Prieur, L. Martel, J.-F. Vigier, A.C. Scheinost, K.O. Kvashnina, J. Somers, Ph. Martin, Aliovalent Cation Substitution in UO_2: Electronic and Local Structures of $U_{1-y}La_yO_{2\pm x}$ Solid Solutions, Inorg. Chem. 57 (2018) 1535–1544.

[19] B.T.M. Willis, The defect structure of hyperstoichiometric uranium dioxide, Acta Cryst. A34 (1978) 88–90.

[20] J.M. Elorrieta, L.J. Bonales, N. Rodriguez-Villagra, V.G. Baonza, J. Cobos, A detailed Raman and X-ray study of UO_{2+x} oxides and related structure transitions, Phys. Chem. Chem. Phys. 18 (2016) 28209-28216.

[21] Ch. Riglet-Martial, Ph. Martin, D. Testemale, C. Sabathier-Devals, G. Carlot, P. Matheron, X. Iltis, U. Pasquet, C. Valot, C. Delafoy, R. Largenton, Thermodynamics of chromium in UO_2 fuel: A solubility model, J. Nucl. Mater. 447 (2014) 63–72.

[22] C. Mieszczynski, G. Kuri, J. Bertsch, M. Martin, C.N. Borca, Ch. Delafoy, E. Simoni, Microbeam X-ray absorption spectroscopy study of chromium in large-grain uranium dioxide fuel, J. Phys. Condens. Matter 26 (2014) 355009.

[23] S.C. Middleburgh, D.C. Parfitt, R.W. Grimes, B. Dorado, M. Bertolus, P.R. Blair L. Hallstadius, K. Backman, Solution of trivalent cations into uranium dioxide, J. Nucl. Mater. 420 (2012) 258–261.

[24] Z. Guo, R. Ngayam-Happy, M. Krack, A. Pautz, Atomic-scale effects of chromium-doping on defect behaviour in uranium dioxide fuel, J. Nucl. Mater. 488 (2017) 160–172.

[25] D.M. Smyth, The defect chemistry of metal oxides, Oxford University Press, New York & Oxford, 2000.

[26] H. Kleykamp, The solubility of selected fission products in UO_2 and $(U, Pu)O_2$, J. Nucl. Mater. 206 (1993) 82–86.

[27] R.G. Berman, T.H. Brown, A thermodynamic model for multicomponent melts, with application to the system CaO-A1$_2$O$_3$-SiO$_2$, Geochim. Cosmochim. Acta 48 (1984) 661–678.

[28] R.G. Berman, Internally-consistent thermodynamic data for minerals in the system Na_2O-K_2O-CaO-MgO-FeO-Fe_2O_3-Al_2O_3-SiO_2-TiO_2-H_2O-CO_2, J. Petrol. 29(2) (1988) 445–522.

[29] B.J. Wood, J. Nicholls, The thermodynamic properties of reciprocal solid solutions, Contrib. Mineral. Petrol. 66 (1978) 389–400.

[30] B. Sundman, J. Ågren, A regular solution model for phases with several components and sublattices suitable for computer applications, J. Phys. Chem. Solids 42 (1981) 297–301.

[31] M. Hillert, The compound energy formalism, J. Alloy. Compd. 320 (2001) 161–176.

[32] P. Richet, The physical basis of thermodynamics: with applications to chemistry, Springer, New York, 2001.

[33] J. Ganguly, Thermodynamics in Earth and Planetary Sciences, Springer, Berlin, 2008.

[34] M. Hillert, Phase Equilibria, Phase Diagrams and Phase Transformations, Second Edition, Cambridge University Press, 2008.

[35] H.L. Lukas, S.G. Fries, B. Sundman, The CALPHAD method, Cambridge University Press, New York, 2007.

[36] Ch. Guéneau, N. Dupin, B. Sundman, Ch. Martial, J.-Ch. Dumas, S. Gossé, S.Chatain, F. De Bruycker, D. Manara, R.J.M. Konings ,Thermodynamic modelling of advanced oxide and carbide nuclear fuels: Description of the U–Pu–O–C systems, J. Nucl. Mater. 419 (2011) 145–167.

[37] P.-Y. Chevalier, E. Fischer, B. Cheynet, Progress in the thermodynamic modelling of the O–U binary system, J. Nucl. Mater. (2002) 303 1–28.

[38] W.T. Thompson, B.J. Lewis, E.C. Corcoran, M.H. Kaye, S.J. White, F. Akbari, Z. He, R. Verrall, J.D. Higgs, D.M. Thompson, T.M. Besmann, S.C. Vogel, Thermodynamic treatment of uranium dioxide based nuclear fuel, Int. J. Mater. Res. 98(10) (2007) 1004–1011.

[39] NEA Nuclear Science Committee, Thermodynamics of Advanced Fuels e International Database (TAF-ID) (n.d.), https://www.oecd-nea.org/science/taf-id/ (Accessed 21 January 2020).

[40] B. Cheynet, E. Fischer, MEPHISTA: A thermodynamic database for new generation nuclear fuels. HAL archive, 2007, https://hal.archives-ouvertes.fr/hal-00222025 (Accessed 21 January 2020).

[41] W.T. Thompson, B.J. Lewis, M.H. Piro, E.C. Corcoran, M.H. Kaye, J.D. Higgs, F. Akbari, D.M. Thompson, RMC Fuel Thermochemical Treatment, an online appendix

to B.J. Lewis, W.T. Thompson, F.C. Iglesias, Fission Product Chemistry in Oxide Fuels in: R.J.M. Konings (Eds.), Comprehensive Nuclear Materials, Elsevier, 2012.

[42] N. Ch. Baenziger, The crystal structures of some thorium and uranium compounds, Ph.D. thesis, Iowa State University, Digital Repository, Retrospective Theses and Dissertations 13190, 1948.

[43] X. Guo, E. Tiferet, Q. Liang, J.M. Solomon, A. Lanzirotti, M. Newville, M.H. Engelhard, R.K. Kukkadapu, D. Wu, E.S. Ilton, M. Asta, S.R. Sutton, H. Xua, A. Navrotsky, U(V) in metal uranates: a combined experimental and theoretical study of $MgUO_4$, $CrUO_4$, and $FeUO_4$, Dalton Trans. 45 (2016) 4622–4632.

[44] R. Guillaumont, T. Fanghänel, V. Neck, J. Fuger, D.A. Palmer, I. Grenthe, M.H. Rand, Update on the Chemical Thermodynamics of Uranium, Neptunium, Plutonium, Americium and Technetium, F.J. Mompean et al. (Eds.), Chemical Thermodynamics Vol. 5, Nuclear Energy Agency, Elsevier, Amsterdam, 2003.

[45] E.H.P. Cordfunke, R.J.M. Konings, Thermochemical data for reactor materials and fission products, North Holland, Amsterdam, 1990.

[46] D.J.M. Bevan, I.E. Grey, B.T.M. Willis, The crystal structure of β-U_4O_{9-y}, J. Solid State Chem. 61 (1986) 1–7.

[47] L. Desgranges, G. Baldinozzi, D. Siméone, H.E. Fischer, Refinement of the α-U_4O_9 Crystalline Structure: New Insight into the U_4O_9 - U_3O_8 Transformation, Inorg. Chem. 50 (2011) 6146–6151.

[48] A. Nakamura, T. Fujino, Thermodynamic study of UO_{2+x} by solid state EMF technique, J. Nucl. Mater. 149 (1987) 80–100.

[49] G.D. Miron, D.A. Kulik, S.V. Dmytrieva, Th. Wagner, GEMSFITS: Code package for optimization of geochemical model parameters and inverse modeling, Appl. Geochem. 55 (2015) 28–45.

[50] J. Spino, P. Peerani, Oxygen stoichiometry shift of irradiated LWR-fuels at high burn-ups: Review of data and alternative interpretation of recently published results, J. Nucl. Mater. 375 (2008) 8–25.

[51] K. Une, M. Oguma, Oxygen potentials of $(U,Nd)O_{2\pm x}$ solid solutions in the temperature range 1000-1500 ^{o}C, J. Nucl. Mater. 118 (1983) 189–194.

[52] T. Matsui, K. Naito, Electrical conductivity measurement and thermogravimetric study of lanthanum-doped uranium dioxide, J. Nucl. Mater. 138 (1986) 19–26.

[53] K. Hagemark, M. Broli, Equilibrium Oxygen Pressures Over Solid Solutions of Urania-Yttria and Urania-Lanthana at 1100°C to 1400°C, J. Am. Ceram. Soc. 50(11) (1967) 563–567.

[54] E. Stadlbauer, U. Wichmann, U. Lott, C. Keller, Thermodynamics and Phase Relationships of the Ternary Lanthanum-Uranium-Oxygen System, J. Solid State Chem. 10(4) (1974) 341–350.

[55] K.W. Bagnall, Recent Advances in Actinide and Lanthanide Chemistry, in: P.R. Fields, Th. Moeller (Eds.), Advances in Chemistry Vol. 71, 1967, pp. 1–12.

[56] L. Eyring, Fluorite-Related Oxide Phases of the Rare Earth and Actinide Elements, in: P.R. Fields, Th. Moeller (Eds.), Advances in Chemistry Vol. 71, 1967, pp. 67–85.

[57] H. Kleykamp, The chemical state of the fission products in oxide fuels, J. Nucl. Mater. 131 (1985) 221–246.

[58] M.H. Kaye, A Thermodynamic Model for Noble Metal Alloy Inclusions in Nuclear Fuel Rods and Application to the Study of Loss-of-Coolant Accidents, Doctoral thesis, Queen's University, Canada, 2001.

[59] M.H. Kaye, B.J. Lewis, W.T. Thompson, Thermodynamic treatment of noble metal fission products in nuclear fuel, J. Nucl. Mater. 366 (2007) 8–27.

[60] D. Cui, V.V. Rondinella, J.A. Fortner, A.J. Kropf, L. Eriksson, D.J. Wronkiewicz, K. Spahiu, Characterization of alloy particles extracted from spent nuclear fuel, J. Nucl. Mater. 420 (2012) 328–333.

[61] E.H.P. Cordfunke, R.J.M. Konings, Chemical interactions in water-cooled nuclear fuel: a thermochemical approach, J. Nucl. Mater. 152 (1988) 301–309.

[62] K.H. Neeb, The Radiochemistry of Nuclear Power Plants with Light Water Reactors, Walter de Gruyter, Berlin, 1997, p.123.

[63] C. Ferry, Ch. Poinssot, V. Broudic, Ch. Cappelaere, L. Desgranges, Ph. Garcia, Ch. Jégou, P. Lovera, P. Marimbeau, J.-P. Piron, A. Poulesquen, D. Roudil, Synthesis on the long term spent fuel evolution, Report CEA-R-6084, Commissariat à l'Energie Atomique (CEA), France, 2004.

[64] Nucleonica, https://nucleonica.com/index.aspx (Accessed 24 January 2020).

[65] Hj. Matzke, Oxygen potential measurements in high burnup LWR UO_2 fuel, J. Nucl. Mater. 223 (1995) 1–5.

[66] Ph. Déhaudt, Le combustible nucléaire et son état physico-chimique à la sortie des réacteurs, CEA Report CEA-R-5923, Commissariat à l'Energie Atomique (CEA), France, 2000.

[67] C. Ciszak, Etude de l'accrochage pastille/gaine des crayons combustibles des réacteurs à eau pressurisée, Ph.D. thesis, Université Bourgogne-Franche-Compté, France, 2017.

[68] V. Rondinella, Oxygen potential of high burnup UO_2, 2015 American Nuclear Society Annual Meeting Proc. Vol. 112 (2015) 397–399.

[69] K. Une, Y. Tominaga, S. Kashibe, Oxygen Potentials and Lattice Parameter of Irradiated BWR Fuels, J. Nucl. Sci. Technol. 28(5) (1991) 409–417.

[70] C.T. Walker, V.V. Rondinella, D. Papaioannou, S. Van Winckel, W. Goll, R. Manzel, On the oxidation state of UO_2 nuclear fuel at a burn-up of around 100 MWd/kgHM, J. Nucl. Mater. 345 (2005) 192–205.

[71] T. Ohmichi, S. Fukushima, A. Maeda, H. Watanabe, On the relation between lattice parameter and O/M ratio for uranium dioxide-trivalent rare earth oxide solid solution, J. Nucl. Mater. 102 (1981) 40–46.

[72] L. Desgranges, Y. Pontillon, P. Matheron, M. Marcet, P. Simon, G. Guimbretière, F. Porcher, Miscibility Gap in the U−Nd−O Phase Diagram: A new Approach of Nuclear Oxides in the Environment? Inorg. Chem. 51 (2012) 9147−9149.

[73] I. Barin, Thermodynamic data of pure substances, Third Edition, VCH Verlagsgesellschaft, Weinheim, Germany, 1995.

[74] Y. Jeannin, C. Mannerskantz, F.D. Richardson, Activities in Iron-Chromium Alloys, Trans. Metallurgical Soc. AIME 227 (1963) 300–305.

[75] N.Y. Toker, L.S. Darken, A. Muan, Equilibrium Phase Relations and Thermodynamics of the Cr-O System in the Temperature Range of 1500 ºC to 1825 ºC, Metallurgical Trans. B 22B (1991) 225–232.